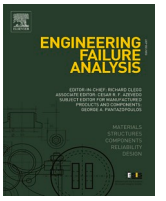
Engineering Failure Analysis 190 (2026) 110746



Contents lists available at ScienceDirect

Engineering Failure Analysis

journal homepage: www.elsevier.com/locate/engfailanal



# Dynamic failure mechanisms of anchored rock mass in complex geology: Insights from laboratory experiments and FDM–DEM coupled numerical simulations

Xiaofeng Qin [a], Haijian Su [a,*], Liyuan Yu [a], Thi Nhan Pham [b], Wei Li [a], Bowen Hu [a]

[a] State Key Laboratory of Intelligent Construction and Healthy Operation and Maintenance of Deep Underground Engineering, China University of Mining and Technology, Xuzhou 221116, China
[b] Faculty of Civil Engineering, Hanoi University of Mining and Geology, Hanoi 100000, Viet Nam

ARTICLE INFO

*Keywords:*
Structural planes
Dynamic failure
Stress-wave propagation
Anchorage failure mechanisms
FDM–DEM coupling

ABSTRACT

To investigate the dynamic failure behavior of anchored rock mass in complex geological structures, this work performed dynamic loading tests on anchored unit cells containing different structural planes (bedding and fracture surfaces). A coupled finite difference–discrete element numerical simulation was further employed to examine the effects of structural planes on the dynamic response of the specimens from both the surrounding rock and bolt perspectives, and to elucidate the failure mechanisms of the anchoring system. The main conclusions are as follows. Fracture surfaces play a dominant role in controlling the loading rate, peak load, and energy dissipation of the anchored units, and this effect is negatively correlated with Joint roughness coefficient (*JRC*). The peak load of anchored units containing a rough fracture surface ($JRC = 16$) reaches 74.69% of that for intact specimens, whereas that of units with a smooth fracture surface ($JRC = 0$) is only 22.58%. The propagation path of the disturbance stress wave is jointly governed by the fracture surface (primary) and bedding planes (secondary), with the most pronounced wave deflection occurring at the fracture surface. Bedding angle influences crack propagation by modulating wave velocity and reflection paths. Secondary cracks preferentially develop along bedding planes, and the dominant failure modes of both the anchored unit and the bolt are primarily controlled by fracture-surface characteristics. These findings improve the understanding of dynamic instability mechanisms and provide support for anchoring system design.

## 1. Introduction

Rock bolting, as one of the most widely adopted methods for controlling surrounding rock deformation, has been extensively applied in rock engineering, including highway tunnels and coal mine roadways. Existing studies indicate that the performance of rock bolting is influenced not only by the intrinsic parameters (e.g., bolt type, geometry dimensions, and pretensioning force) [1–3], but also by the geological structural characteristics of the surrounding rock and the external loads acting on it. In particular, under the typical “three highs and one disturbance” conditions in deep coal mining [4], the surrounding rock experiences long-term coupled effects of high in-situ stress, high energy accumulation, and intense dynamic disturbances, leading to pronounced structural complexity. Under such conditions, dynamic loads—such as blasting-induced disturbances, mechanical rock fragmentation, and

* Corresponding author.
*E-mail address:* hjsu@cumt.edu.cn (H. Su).

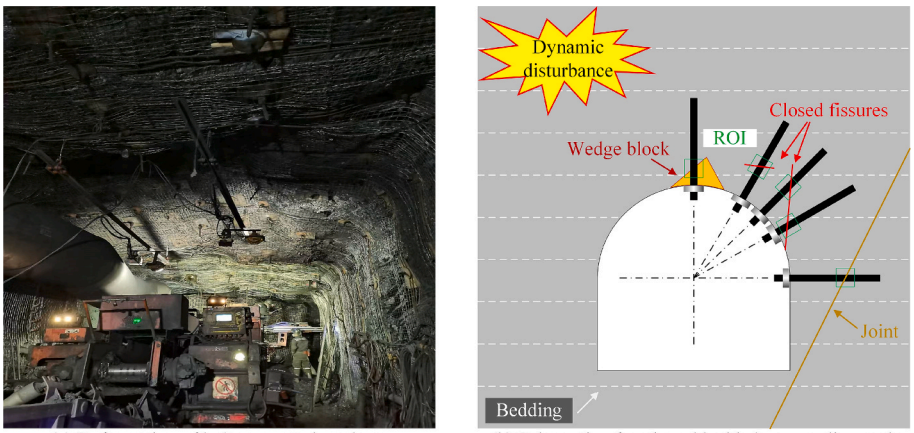
https://doi.org/10.1016/j.engfailanal.2026.110746
Received 16 December 2025; Received in revised form 5 March 2026; Accepted 7 March 2026
Available online 8 March 2026
1350-6307/© 2026 Elsevier Ltd. All rights are reserved, including those for text and data mining, AI training, and similar technologies.

**Nomenclature**

| | |
|---|---|
| $A_B$ | Cross-sectional area of the incident and transmitted bars. |
| $B$ | Thickness of the specimen. |
| $D$ | Geometric fractal dimension of fracture surfaces. |
| $E_a$, $E_b$, $E_d$, $E_k$, $E_s$ | Strain energy, bond energy, damping energy, kinetic energy, and slip energy, respectively. |
| $E_B$ | Elastic modulus of the incident and transmitted bars. |
| $F$ | $F$-statistic. |
| $h$ | Tooth height of the serrated fracture surface. |
| $H$ | Height of the specimen |
| $JRC$ | Joint roughness coefficient. |
| $K$ | Loading rate. |
| $l$ | Tooth spacing of the serrated fracture surface. |
| $L$ | Length of the specimen. |
| $m_5$ | Mass of fragments with a particle size $< 5$ mm. |
| $p$ | $p$-value (significance level). |
| $p_{bp}$, $p_{sp}$ | Peak bolt axial force and bolt axial force at the specimen load peak time, respectively. |
| $P$, $P_{sp}$ | Applied load on the specimen and peak applied load, respectively. |
| $SS$ | Sum of squares |
| $t_{bp}$, $t_{sp}$ | Time corresponding to the peak bolt axial force and the peak specimen load, respectively. |
| $T$ | Period of the incident stress wave |
| $U$, $U_e$, $U_d$ | Total energy, elastic energy, and dissipated energy, respectively. |
| $V$, $V_0$ | Velocity applied to the grid nodes and peak velocity, respectively. |
| $\alpha$ | Bedding dip angle. |
| $\eta^2$ | Effect size (variance explained). |
| $\varepsilon_I(t)$, $\varepsilon_R(t)$, $\varepsilon_T(t)$ | Incident, reflected, and transmitted strain time histories, respectively. |
| $\Phi$ | Diameter of the hole. |

periodic roof fracturing—frequently act on the rock bolting system. Consequently, the load-bearing capacity of the anchored surrounding rock structure is significantly reduced, and rock bolts become more susceptible to failure, which may trigger surrounding rock instability (Fig. 1a). Therefore, a systematic understanding of the dynamic mechanical response of anchored surrounding rock units under complex geological structural conditions is of considerable engineering significance for evaluating rock bolting performance and optimizing support design in deep underground engineering.

Regarding the mechanical behavior of the surrounding rock–bolt anchorage system, extensive work has treated the anchored unit as the fundamental object of investigation. Laboratory experiments have been widely employed to examine the evolution of anchorage performance under various external loading conditions, including cyclic pull-out tests [5], cyclic shear loading tests [6], static compression tests [7], and dynamic tensile tests [8]. Existing results suggest that anchorage performance may deteriorate appreciably under dynamic loading, depending on loading conditions and structural configuration. For example, Khaleghparast et al. [9] reported, based on a comparison between static and dynamic shear loading, that the dynamic shear strength of an anchored unit is




(a) Deformation of bolt-supported roadway surrounding rock subjected to mining activities

(b) Schematic of anchored bedded surrounding rock with a through-going fracture

**Fig. 1.** Bolt-supported surrounding rock under dynamic disturbance.

approximately 70% of its static value. In recent years, research on the dynamic response of anchored structures in deep underground engineering has expanded from single loading modes to more complex stress environments. These studies include, for instance, the inhibitory effect of rock bolts on dynamic damage evolution [10], performance differences associated with varying anchorage lengths under combined static and dynamic loads [11], and dynamic response characteristics under true triaxial stress conditions [12]. In addition, increasing attention has been devoted to the energy evolution and failure criteria of anchorage systems under high strain-rate conditions [13–15], as well as to damage evolution mechanisms of the bolt–surrounding rock interface under dynamic loading [16–18].

Although the aforementioned studies have provided relatively systematic investigations into external load types and loading modes, most of the existing work still treats the surrounding rock as a homogeneous or simplified medium, with insufficient attention to the coupled effects between surrounding rock geological structures and the dynamic response of the anchorage system. As a typical sedimentary rock mass, coal-measure strata are commonly characterized by well-developed bedding. Owing to tectonic activity, bedding dip angle varies over a wide range and exhibits complex spatial distributions. Previous studies have demonstrated that bedding orientation exerts a significant influence on rock dynamic mechanical properties. For instance, Feng et al. [19] reported pronounced anisotropy in shale dynamic tensile strength; Wang et al. [20] found that the dynamic crack initiation stress intensity factor of coal decreases with increasing bedding dip angle, and that crack propagation direction is strongly controlled by bedding; Chang et al. [21] further revealed that these bedding effects depend on loading rate, with cracks tending to propagate along bedding planes under static loading, whereas crack propagation becomes considerably more complex under dynamic loading. An increasing number of studies have incorporated bedding as an important consideration in the mechanical analysis of anchored surrounding rock structures. Li et al. [22] investigated the influence of shale bedding dip angle on the strength characteristics of anchored specimens. Lu et al. [23] discussed the effective conditions of rock bolting in bedded rock masses under impact loading, as well as the mechanisms governing crack control and evolution. Sun et al. [24] reported the bedding effects in bedded rock masses supported by cable anchorage systems.

In addition to bedding, surrounding rock masses commonly contain structural discontinuities—including pores, fractures, and joints—which likewise play a crucial role in governing the stability of anchored surrounding rock structures. Existing studies have demonstrated that the geometric characteristics of pre-existing fractures can significantly modify the dynamic load-bearing behavior and failure modes of anchored systems. For instance, Fan et al. [13] reported that anchorage performance exhibits a quadratic increase as the angle between the rock bolt and the fracture plane decreases, while Chen et al. [16] further elucidated the controlling effect of fracture orientation on microcrack initiation and propagation paths. In recent years, increasing attention has been directed to the dynamic response of rock masses with coexisting structural features, such as porous bedded sandstones [25] and layered gneisses containing filled joints [26]. Nevertheless, these studies have predominantly focused on the dynamic failure behavior of the rock mass itself. Investigations addressing the coupled effects of multiple structural discontinuities under anchored conditions remain relatively scarce, particularly systematic analyses of how complex fracture morphologies influence the dynamic mechanical response of anchored surrounding rock structures.

Particular attention should be paid to through-going fractures, which are widely distributed in loose or highly fractured surrounding rock masses and constitute a critical hazard that may induce large deformation and surrounding rock instability [27,28].

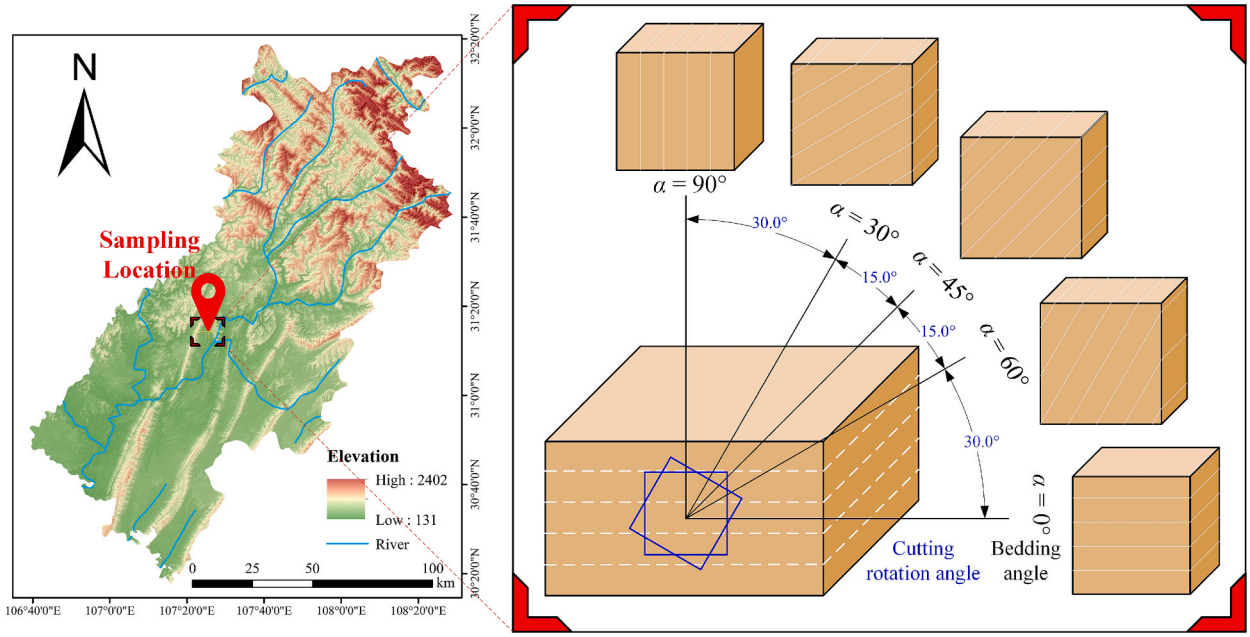



**Fig. 2.** Schematic diagram of the sampling location and sampling procedure.

Existing work on the dynamic mechanical response of anchorage systems has mainly focused on intact rock masses or those containing non–through-going discontinuities. In contrast, a systematic understanding of the mechanical response, failure modes, and the synergistic effects with bedding in anchored surrounding rock structures containing through-going fractures (Fig. 1b) under dynamic loading remains limited. Meanwhile, although the finite element–discrete element (FEM–DEM) coupling method has developed rapidly in recent years for analyzing dynamic failure in structural systems [29–31], its application to elucidating dynamic failure mechanisms of anchored surrounding rock structures with complex structural features remains relatively limited.

Based on the above considerations, investigates rock specimens with well-developed bedding and different through-going fracture morphologies under anchored conditions. Dynamic loading tests are performed on specimens without through-going fractures, with linear through-going fractures, and with serrated through-going fractures. Combined with FEM–DEM coupled numerical simulations, this work systematically examines the effects of through-going fracture morphology and bedding dip angle on the dynamic mechanical response and failure evolution of anchored surrounding rock units. The outcomes of this work aim to provide a theoretical basis for the design and safety assessment of rock bolting support in surrounding rock masses with complex geological structures, including bedding and through-going fractures, in deep underground engineering.

## 2. Experimental design

### 2.1. Specimen production

#### 2.1.1. Sampling of rock specimens and analysis of mineral composition

All rock specimens used in this work were collected from a quarry in Dazhou, Sichuan Province, China (Fig. 2). To reduce variability in test results arising from natural heterogeneity, all specimens were obtained from the same parent rock. The parent rock exhibits a light-yellow matrix and white bedding, which is uniformly distributed throughout the material. The average density is 2299 kg/m$^3$, and the primary mineral constituents are quartz (98.5%) and clay minerals (1.5%), indicating that the material is a typical quartz sandstone. The detailed XRD results are presented in Fig. 3. By adjusting the cutting angle, the angle between bedding and the specimen ends was controlled, and initial rock blocks with bedding dip angles ($\alpha$) of 0°, 30°, 45°, 60°, and 90° were prepared (Fig. 2). Each block had approximate dimensions of 100 mm × 100 mm × 100 mm to allow for subsequent cutting and machining.

#### 2.1.2. Preparation of anchored units

To investigate the dynamic mechanical behavior of anchored units in surrounding rock masses with complex geological structures, the region of interest in Fig. 1 was selected as the prototype. A simplified unit was then developed from this prototype for testing, as illustrated in Fig. 4f. The initial rock blocks were further processed by wire cutting to obtain specimens measuring 80 mm (length) × 80 mm (height) × 40 mm (thickness). A 4 mm-diameter through-hole was subsequently drilled to complete the Type A unit (without a through-going fracture), as shown in Fig. 4a.

Based on the Type A unit, two additional types of surrounding-rock units containing through-going fractures were produced by wire cutting along the diagonal direction at 45°: (i) Type B with a smooth fracture surface and (ii) Type C with a serrated fracture surface. The geometric configurations of the fracture surfaces are shown in Fig. 4b. The serrated configuration is commonly used to control the roughness of artificial fracture surfaces [32], and specific roughness levels can be achieved by adjusting serration geometry. According to Eqs. (1) and (2) proposed by Xie and Pariseau [33], the joint roughness coefficient (*JRC*) of the Type C fracture surface was determined to be 16.

$$D = \lg 4/\lg\{2[1+\cos(\arctan(2h/l))]\} \tag{1}$$

$$JRC = 85.2671(D-1)^{0.5679} \tag{2}$$

where, D represents the geometric fractal dimension of the fracture surface, h denotes the tooth height, and l denotes the tooth spacing. The anchored surrounding rock units with different bedding dip angles are shown in Fig. 4c. With reference to bolt dimensions

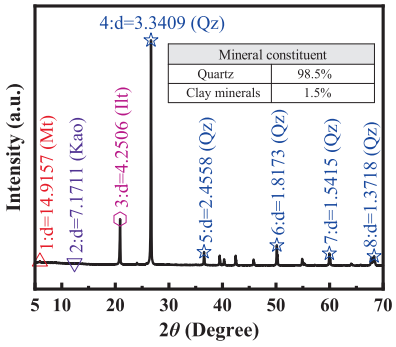



**Fig. 3.** Mineral composition of the rock specimens based on XRD analysis.

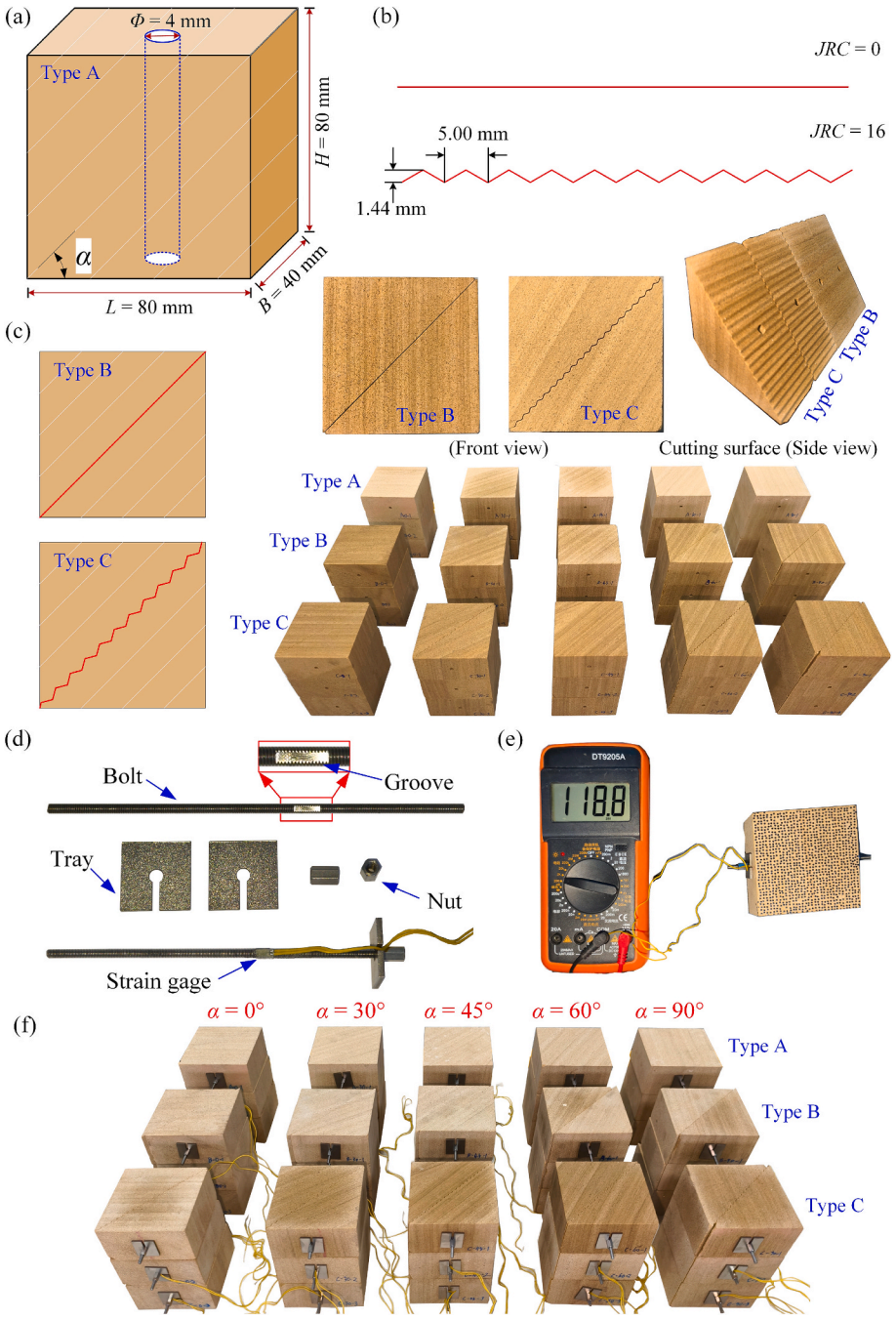



**Fig. 4.** Preparation of the specimens: (a) schematic diagram of the specimen geometry; (b) schematic of the fracture surface geometry; (c) specimen after machining the structural surface; (d) schematic of the bolt components; (e) resistance check of the strain gauge after bolt assembly; (f) completed specimen.

commonly used in mine roadways, a scale factor of 10 was applied. Following the design principles adopted by Ren et al. [34], a 3 mm-diameter threaded rod was selected as the bolt body. A square washer with a side length of 20 mm (thickness 2 mm, hole diameter 3 mm, and slot width 1.5 mm) was used as the tray, and an 8-mm-long metric M3 hex nut was used as the fastening nut. To monitor the evolution of bolt axial force, a 0.2 mm-deep groove was machined 10 mm from the bolt center, and a strain gauge (BF120-2AA) was bonded at this location, as shown in Fig. 4d. After confirming with a multimeter that the strain gauge was not short-circuited, a pretensioning force of 1.5 kN was applied to the bolt using a torque wrench. The completed anchored unit is shown in Fig. 4f.

To determine the pretensioning torque, a bolt load cell was used to measure axial force under different applied torque levels, as shown in Fig. 5a. The results indicated that a torque of 1.2 N·m produces a bolt pretensioning force of 1.5 kN. To identify the reliable

measurement range of the strain-gauge method for monitoring bolt axial force [24] and to establish the strain–axial force relationship, a tensile test was performed on the bolt using an electronic universal testing machine. The tensile section length was 80 mm, and the loading rate was 0.2 mm/min, as shown in Fig. 5c. Only a static tensile test was performed to obtain the static elastic modulus, which was used as a surrogate for the dynamic elastic modulus. According to the findings of Kang et al. [35] and Hassel [36], the stiffness and elastic modulus of metallic bolts exhibit minimal differences between static and dynamic loading conditions. Since this work focuses on the dynamic evolution of bolt axial force rather than highly precise absolute values, this simplification is considered acceptable. When bolt tensile deformation exceeded a critical value, strain-gauge readings became distorted and deviated from the reliable operating range for strain-based axial-force monitoring. As shown in Fig. 5d, the reliable monitoring range of the strain gauge used in this work corresponds to strains of 0–1.33%, which is equivalent to a maximum axial force of 3.35 kN.

### 2.2. Equipment and test scheme

The testing system used in this work was based on a split Hopkinson pressure bar (SHPB) apparatus, which introduces stress waves to evaluate the dynamic mechanical response of the anchored units, as shown in Fig. 6. The system consisted of an air gun, a striker, the bar assembly, and a damper, and a measurement system. The striker and bars were manufactured from high-strength alloy steel with a diameter of 100 mm (elastic modulus 210 GPa, Poisson's ratio 0.29, and longitudinal wave velocity 5,188 m/s). The bar assembly comprised an incident bar, a transmitted bar, and an absorbing bar. The striker was 800 mm long, whereas the incident, transmitted, and absorbing bars were 3,000 mm, 3,000 mm, and 1,200 mm long, respectively. The measurement system consisted of a bar dynamic strain acquisition system, a high-speed imaging system, and a bolt dynamic strain acquisition system. The high-speed imaging system comprised two LED lamps (212,500 lx) and a Phantom v611 high-speed camera operating at 67,000 fps. Both dynamic strain acquisition systems were equipped with strain gauges and connected to dynamic strain acquisition instruments (DH5960), each with a maximum sampling rate of 10 MHz.

During testing, the air gun was pressurized to 0.3 MPa to accelerate the striker, producing an average impact velocity of 6.8 m/s. Upon impact with the incident bar, the striker generated a stress wave, which was shaped into a near half-sine pulse by the pulse

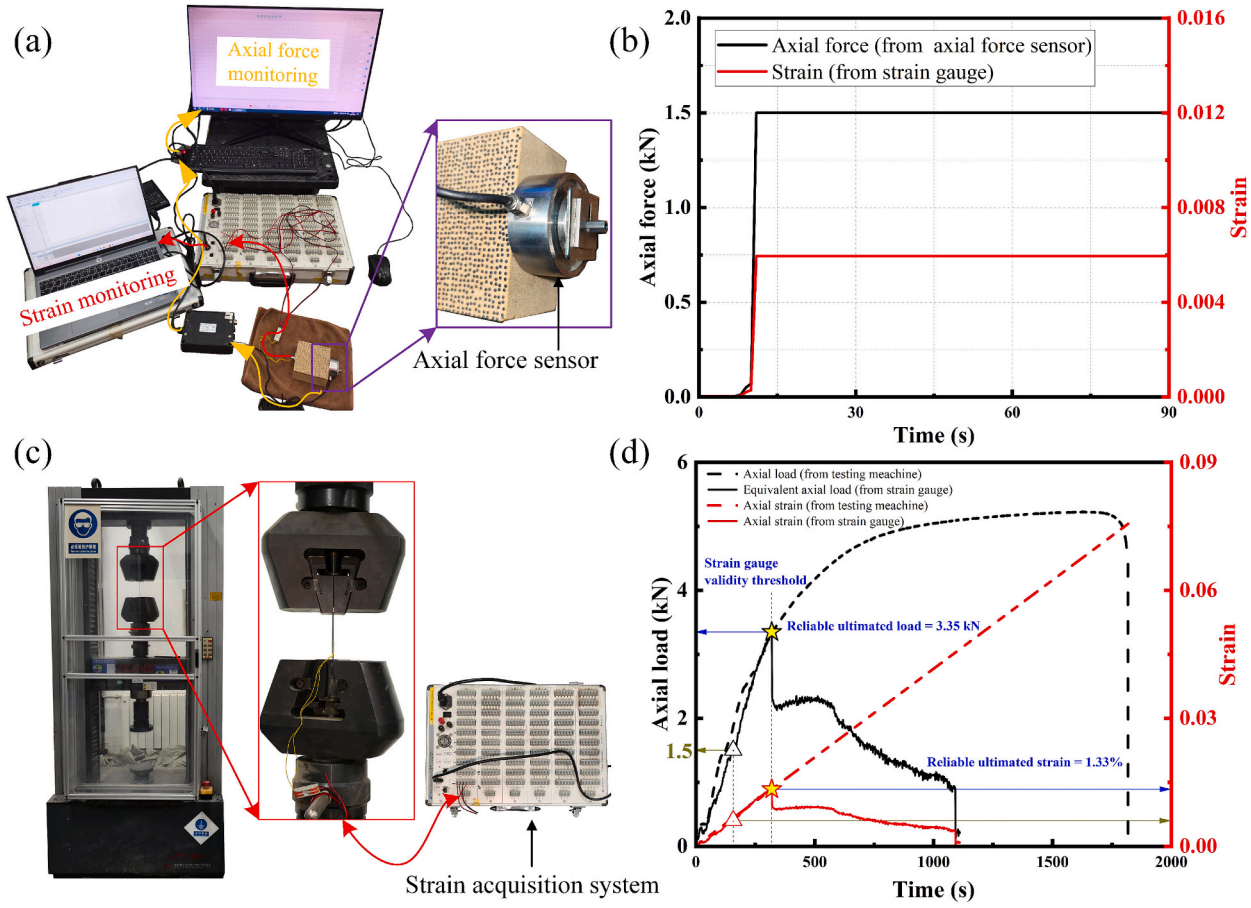



**Fig. 5.** Bolt torque and tensile tests: (a) torque measurement; (b) time history of axial force monitoring; (c) tensile test; (d) time history of tensile load.

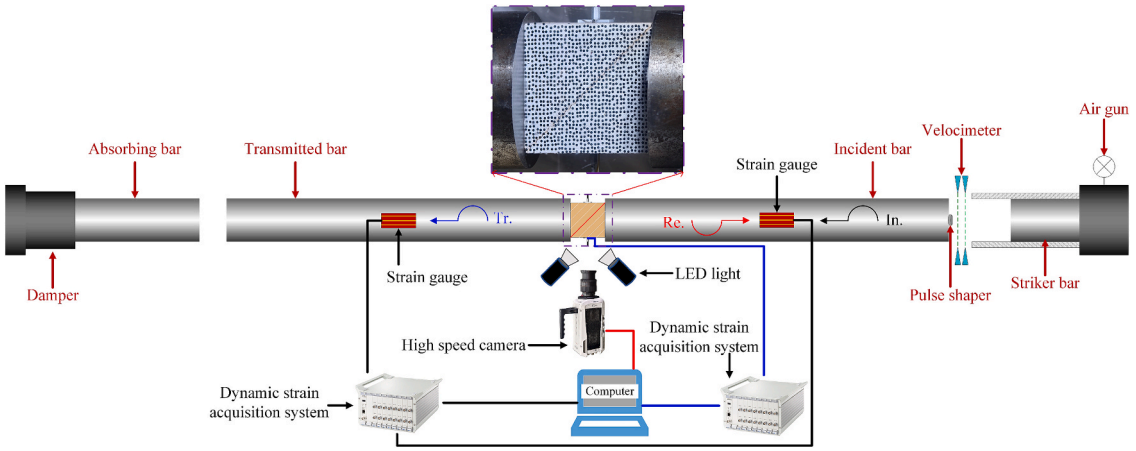



**Fig. 6.** Schematic diagram of the dynamic impact testing system.

shaper. When the stress wave reached the incident bar–specimen interface, part of the wave was transmitted into the specimen, whereas the remainder was reflected back into the incident bar. After propagating through the specimen, the stress wave entered the transmitted bar. Throughout this process, the dynamic strain acquisition system recorded the strain histories of the incident $\varepsilon_I(t)$, reflected $\varepsilon_R(t)$, and transmitted waves $\varepsilon_T(t)$. Based on Eq. (3), the time-dependent load P(t) acting on the specimen was determined [37].

$$P = \frac{A_B E_B}{2}(\varepsilon_I(t) + \varepsilon_R(t) + \varepsilon_T(t)) \tag{3}$$

where, $A_B$ and $E_B$ represent the cross-sectional area and elastic modulus of the bars, respectively. A three-wave consistency check was performed on the recorded data. The close agreement between $\varepsilon_I(t) + \varepsilon_R(t)$ and $\varepsilon_T(t)$ indicates that the loads at both specimen ends were essentially identical, thereby confirming the reliability of the experimental data, as shown in Fig. 7.

## 3. Experimental results and analysis

### 3.1. Influence of fracture surfaces on the mechanical response of bedded anchored units

#### 3.1.1. Mechanical response characteristics of the anchored units

Typical load–time curves of the anchored units with different bedding dip angles are shown in Fig. 8. The presence of fracture surfaces directly affects specimen loading duration. Anchored units containing linear fracture surfaces failed in the shortest time, whereas those without fracture surfaces exhibited the longest loading duration. In terms of curve morphology, specimens with smooth fracture surfaces exhibited a more rapid post-peak load drop, whereas specimens with serrated fracture surfaces generally displayed multiple peaks. The loading rate was influenced by both fracture surfaces and bedding. As shown in Fig. 8d, the presence of fracture surfaces reduced specimen loading rate. The magnitude of this reduction is negatively correlated with the *JRC* value of the fracture surface. The specific values are listed in Table 1. For example, at a bedding dip angle of 0°, the mean loading rate (*K*) of Type C

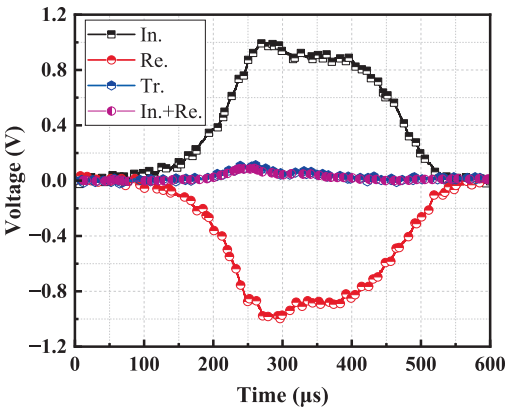



**Fig. 7.** Typical dynamic equilibrium verification.

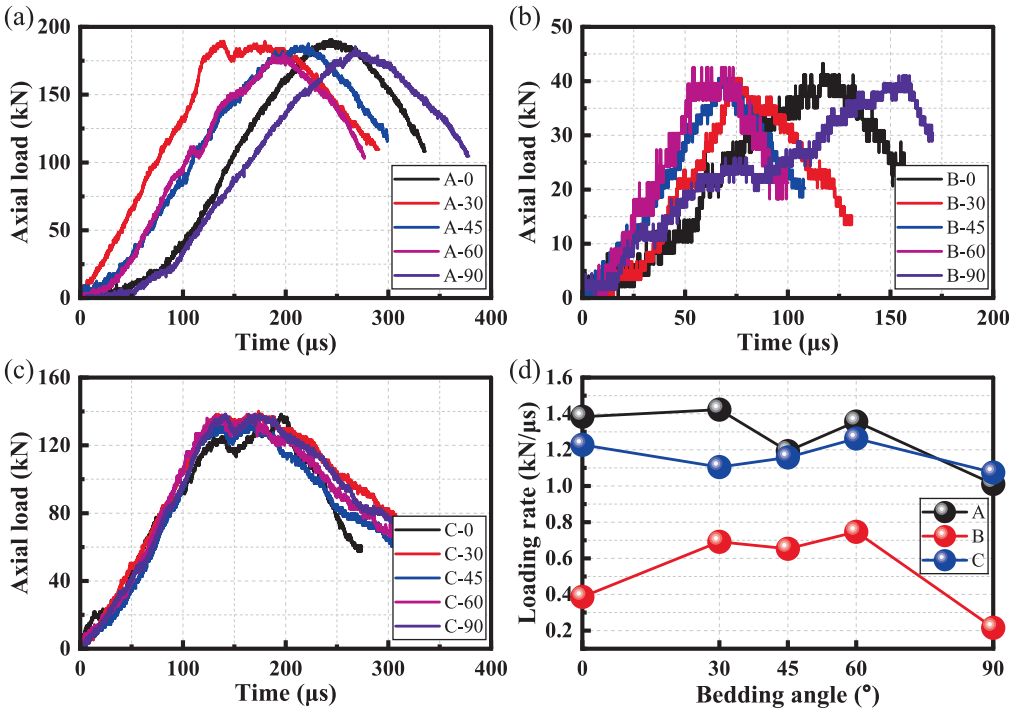



**Fig. 8.** Typical load–time curves: (a) Type A; (b) Type B; (c) Type C.

specimens ($JRC = 16$) was 1.228 kN/μs, which is 11.21% lower than that of Type A specimens without fracture surfaces. The mean loading rate of Type B specimens with linear fracture surfaces ($JRC = 0$) was 0.387 kN/μs, corresponding to only 28.02% of that of Type A specimens. The influence of bedding dip angle varied among specimens with different fracture-surface characteristics. For specimens without fracture surfaces, the mean loading rate was 1.273 kN/μs, with a maximum bedding-induced variation of 20.58% and a variance of 0.03. For specimens with linear fracture surfaces, the mean loading rate was 0.539 kN/μs, with a maximum bedding-induced variation of 59.97% and a variance of 0.05. For specimens with serrated fracture surfaces, the mean loading rate was 1.166 kN/μs, with a maximum bedding-induced variation of 9.76% and a variance of 0.01. A consistent trend across all three specimen groups is that the lowest loading rate occurred at a bedding dip angle of 90°. In addition, bedding effects were most pronounced in specimens containing linear fracture surfaces. This behavior may be associated with stress-wave propagation paths within the specimens, and the underlying mechanism is further examined in Sections 3.3 and 5.2. To quantitatively evaluate the effects of fracture-surface characteristics and bedding dip angle on specimen dynamic mechanical response, a two-way analysis of variance (ANOVA) was performed, as summarized in Table 2. In this analysis, the sum of squares (*SS*) represents data variability; the *F*-value assesses whether between-group differences are statistically significant; the *p*-value indicates the statistical significance level of each factor; and the effect size ($\eta^2$) reflects the proportion of variance in the dependent variable explained by a given independent variable.

Peak load was also influenced by fracture surfaces and bedding dip angle (Fig. 9). Notably, fracture surfaces reduced the bearing capacity of the anchored units, and the magnitude of this reduction was negatively correlated with the *JRC* of the fracture surface. When the bedding dip angle was 0°, the mean peak load was 189.56 kN for specimens without fracture surfaces, 42.80 kN for specimens with linear fracture surfaces ($JRC = 0$), and 141.58 kN for specimens with serrated fracture surfaces ($JRC = 16$). Bedding effects also differed among the three specimen types. For specimens without fracture surfaces, peak load increased first, then decreased, and finally increased slightly with increasing bedding dip angle. The highest bearing capacity occurred at a bedding dip angle of 30°, and the lowest occurred at 60°. For specimens with fracture surfaces, peak load decreased first and then increased with increasing bedding dip angle. For specimens with linear fracture surfaces, the highest bearing capacity occurred at 0° and the lowest at 30°. For specimens with serrated fracture surfaces, the strongest bearing capacity occurred at 90° and the lowest at 45°. Taken together, bedding exerted a smaller overall influence than fracture surfaces.

### *3.1.2. Mechanical response characteristics of the rock bolt*

Based on the bolt axial-force monitoring system, the evolution of bolt axial force under impact loading was obtained, as shown in Fig. 10. By comparing the specimen peak-load time ($t_{sp}$) with the bolt peak axial-force time ($t_{bp}$), it was found that the $t_{bp}$ lagged behind $t_{sp}$ for the anchored unit. That is, after the anchored unit reached its ultimate bearing capacity, the bolt axial force continued to increase. This behavior may be associated with rapid volumetric expansion of the surrounding rock mass after peak failure [34]. The same trend was also observed in the numerical simulations, which helps rule out signal delay in the monitoring system. In addition, bolt axial force in anchored units containing linear fracture surfaces increased continuously throughout the disturbance process.

**Table 1**
Main dynamic response characteristic parameters of the specimens obtained from the laboratory tests.

| No. | Type | $\alpha$/(°) | $K$/(kN/μs) | $P_{sp}$/(kN) | $p_{sp}$/(kN) |
|---|---|---|---|---|---|
| A-0–1 | A | 0 | 1.390 | 190.656 | 3.157 |
| A-0–2 | A | 0 | 1.353 | 185.503 | 2.994 |
| A-0–3 | A | 0 | 1.406 | 192.525 | 3.296 |
| A-30–1 | A | 30 | 1.415 | 190.140 | 3.313 |
| A-30–2 | A | 30 | 1.432 | 192.373 | 3.368 |
| A-30–3 | A | 30 | 1.422 | 189.485 | 3.305 |
| A-45–1 | A | 45 | 1.215 | 190.913 | 3.223 |
| A-45–2 | A | 45 | 1.194 | 187.564 | 3.169 |
| A-45–3 | A | 45 | 1.170 | 183.338 | 3.132 |
| A-60–1 | A | 60 | 1.363 | 185.348 | 3.127 |
| A-60–2 | A | 60 | 1.327 | 180.350 | 2.998 |
| A-60–3 | A | 60 | 1.381 | 187.965 | 3.166 |
| A-90–1 | A | 90 | 1.002 | 183.785 | 3.118 |
| A-90–2 | A | 90 | 1.012 | 185.503 | 3.293 |
| A-90–3 | A | 90 | 1.019 | 185.632 | 3.317 |
| B-0–1 | B | 0 | 0.392 | 43.284 | 1.895 |
| B-0–2 | B | 0 | 0.394 | 43.470 | 1.913 |
| B-0–3 | B | 0 | 0.377 | 41.632 | 1.828 |
| B-30–1 | B | 30 | 0.716 | 41.248 | 1.814 |
| B-30–2 | B | 30 | 0.703 | 40.532 | 1.779 |
| B-30–3 | B | 30 | 0.613 | 35.465 | 1.693 |
| B-45–1 | B | 45 | 0.637 | 39.008 | 1.713 |
| B-45–2 | B | 45 | 0.662 | 40.532 | 1.806 |
| B-45–3 | B | 45 | 0.657 | 40.194 | 1.772 |
| B-60–1 | B | 60 | 0.765 | 42.558 | 2.108 |
| B-60–2 | B | 60 | 0.747 | 41.545 | 2.083 |
| B-60–3 | B | 60 | 0.712 | 39.518 | 2.066 |
| B-90–1 | B | 90 | 0.216 | 41.376 | 1.692 |
| B-90–2 | B | 90 | 0.217 | 41.545 | 1.748 |
| B-90–3 | B | 90 | 0.214 | 41.038 | 1.616 |
| C-0–1 | C | 0 | 1.211 | 138.483 | 2.671 |
| C-0–2 | C | 0 | 1.241 | 141.861 | 2.757 |
| C-0–3 | C | 0 | 1.253 | 144.394 | 2.839 |
| C-30–1 | C | 30 | 1.110 | 140.172 | 2.798 |
| C-30–2 | C | 30 | 1.093 | 137.976 | 2.686 |
| C-30–3 | C | 30 | 1.112 | 139.783 | 2.741 |
| C-45–1 | C | 45 | 1.169 | 137.368 | 2.753 |
| C-45–2 | C | 45 | 1.132 | 132.994 | 2.676 |
| C-45–3 | C | 45 | 1.172 | 137.659 | 2.789 |
| C-60–1 | C | 60 | 1.251 | 136.794 | 2.402 |
| C-60–2 | C | 60 | 1.279 | 139.834 | 2.647 |
| C-60–3 | C | 60 | 1.259 | 137.841 | 2.525 |
| C-90–1 | C | 90 | 1.057 | 138.483 | 2.811 |
| C-90–2 | C | 90 | 1.113 | 145.914 | 2.943 |
| C-90–3 | C | 90 | 1.090 | 143.043 | 2.893 |

**Table 2**
Summary of two-way ANOVA results for assessing the sensitivity of dynamic response parameters to structural plane type and bedding angle.

| | | Structural plane type | Bedding angle | Error |
|---|---|---|---|---|
| $K$ | $SS$ | 3.214 | 0.812 | 0.036 |
| | $F$ | 1443.2 | 91.4 | — |
| | $p$ | <0.001 | <0.001 | — |
| | $\eta^2$ | 0.791 | 0.200 | — |
| $P_{sp}$ | $SS$ | 47164.8 | 1023.6 | 412.5 |
| | $F$ | 2285.6 | 24.8 | — |
| | $p$ | <0.001 | <0.001 | — |
| | $\eta^2$ | 0.968 | 0.021 | — |
| $p_{sp}$ | $SS$ | 8.742 | 0.611 | 0.054 |
| | $F$ | 971.5 | 22.6 | — |
| | $p$ | <0.001 | <0.001 | — |
| | $\eta^2$ | 0.930 | 0.065 | — |
| $U_d$ | $SS$ | 113.214 | 9.862 | 5.938 |
| | $F$ | 76.29 | 3.32 | — |
| | $p$ | <0.001 | 0.067 | — |
| | $\eta^2$ | 0.878 | 0.076 | — |

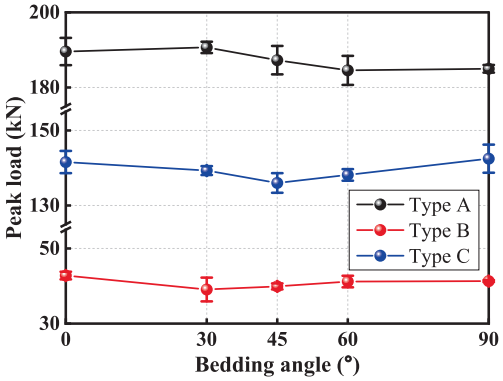



**Fig. 9.** Variation of peak load with bedding dip angle.

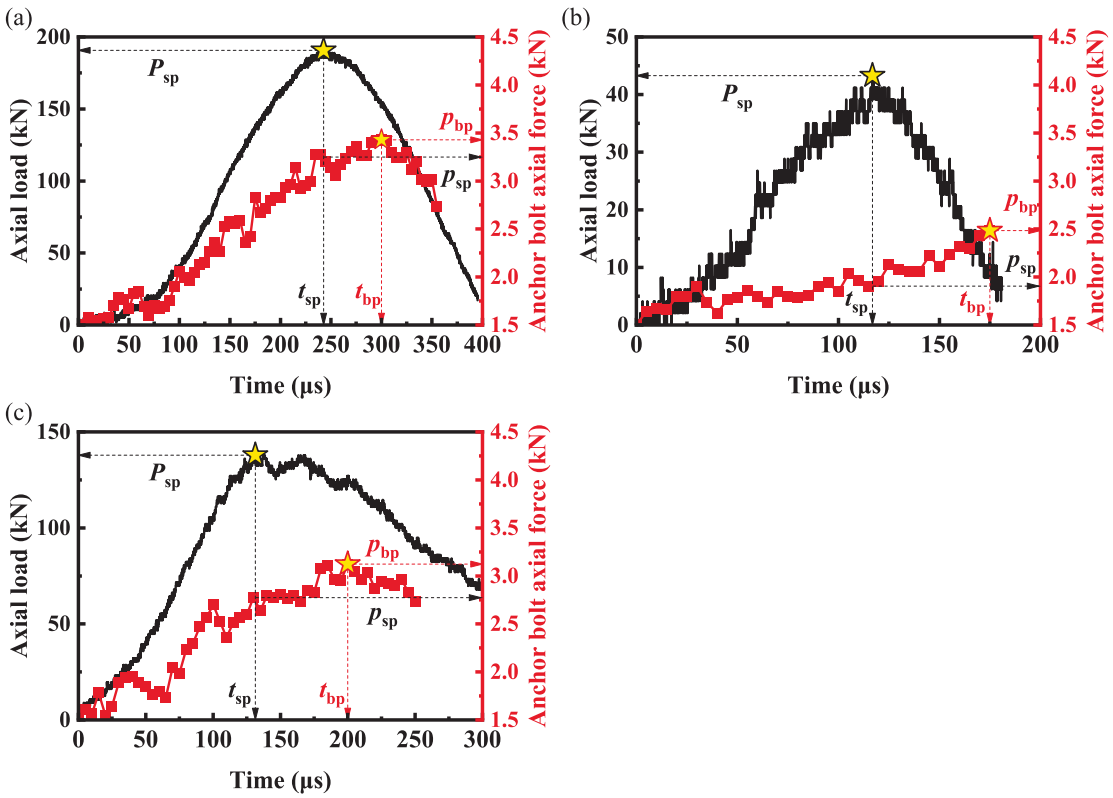



**Fig. 10.** Typical time-history curves of bolt axial force (bedding dip angle of 0°): (a) Type A; (b) Type B; (c) Type C.

Furthermore, the bolt axial force at the specimen peak-load time ($p_{sp}$) was analyzed, as shown in Fig. 11. At a given bedding dip angle, anchored units without fracture surfaces exhibited the highest $p_{sp}$, whereas those containing linear fracture surfaces exhibited the lowest $p_{sp}$. Considering bedding dip angle together with the peak-load failure patterns of the anchored units (Fig. 12), anchoring in units without fracture surfaces was pronounced, as evidenced by clear conical failure zones at both ends of the anchoring region; their failure mode was not predominantly governed by bedding orientation. For anchored units with fracture surfaces, the dependence of $p_{sp}$ on bedding dip angle was more evident, but the dominant mechanisms differed between the two fracture-surface types. For units with linear fracture surfaces, failure mainly occurred along the smooth fracture surface; the bolt provided greater resistance to sliding, and bedding dip angle affected the normal and tangential components of the weak-plane forces. For units with serrated fracture surfaces, mechanical interlocking played a major role, and the interfacial engagement geometry varied with bedding dip angle. A more detailed mechanism analysis is presented in Section 5.2.

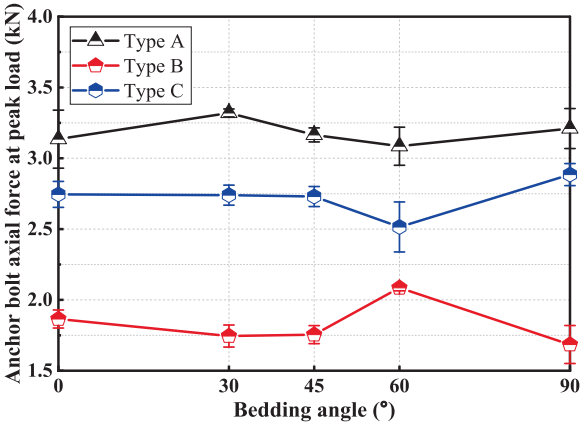



**Fig. 11.** Variation of bolt axial force at the specimen peak-load time with bedding dip angle.

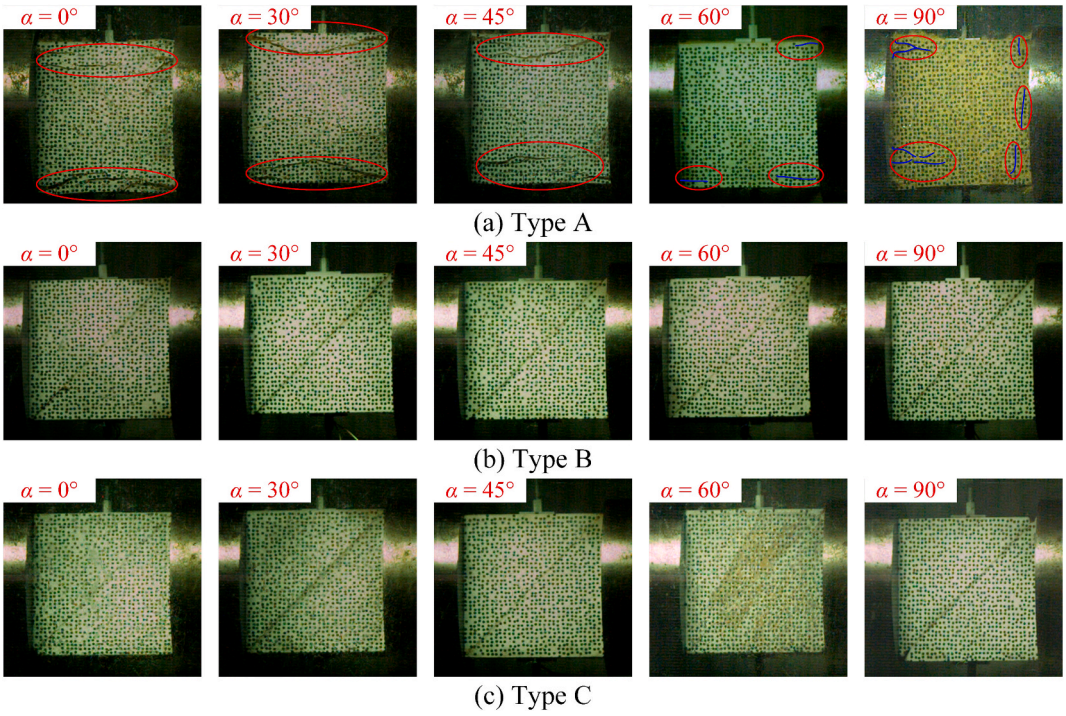



**Fig. 12.** Crack development at the specimen peak-load time: (a) Type A; (b) Type B; (c) Type C.

### 3.2. *Analysis of failure patterns*

The crack development patterns and final failure morphologies of the specimens reflect, to some extent, their failure mechanisms. Fig. 12 shows crack development in the anchored units at the peak load. At peak load, noticeable crack development occurred only in the anchored units without fracture surfaces, and the observed pattern corresponds to the typical end-face failure mode, in which conical failure zones form at both ends of the anchoring section. Bedding-induced crack deflection was also observed. For example, when the bedding dip angle was 0°, conical failure zones were not prominent because horizontal bedding constrained the failure pattern. When the bedding dip angles were 30° and 45°, the inclination of cracks in the upper conical failure zone appeared to be influenced by bedding orientation. When the bedding dip angle was 90°, vertically oriented cracks developed along the bedding plane near the right end. After peak load, the anchored units experienced further instability and failure, and the final failure patterns are shown in Fig. 13. For anchored units without through-going structural planes, overall structural integrity remains relatively high. Under impact loading, the absence of pre-existing discontinuities limits energy release through structural interfaces, leading to repeated reflection and superposition of stress waves within the specimen. Consequently, a considerable portion of the impact energy is

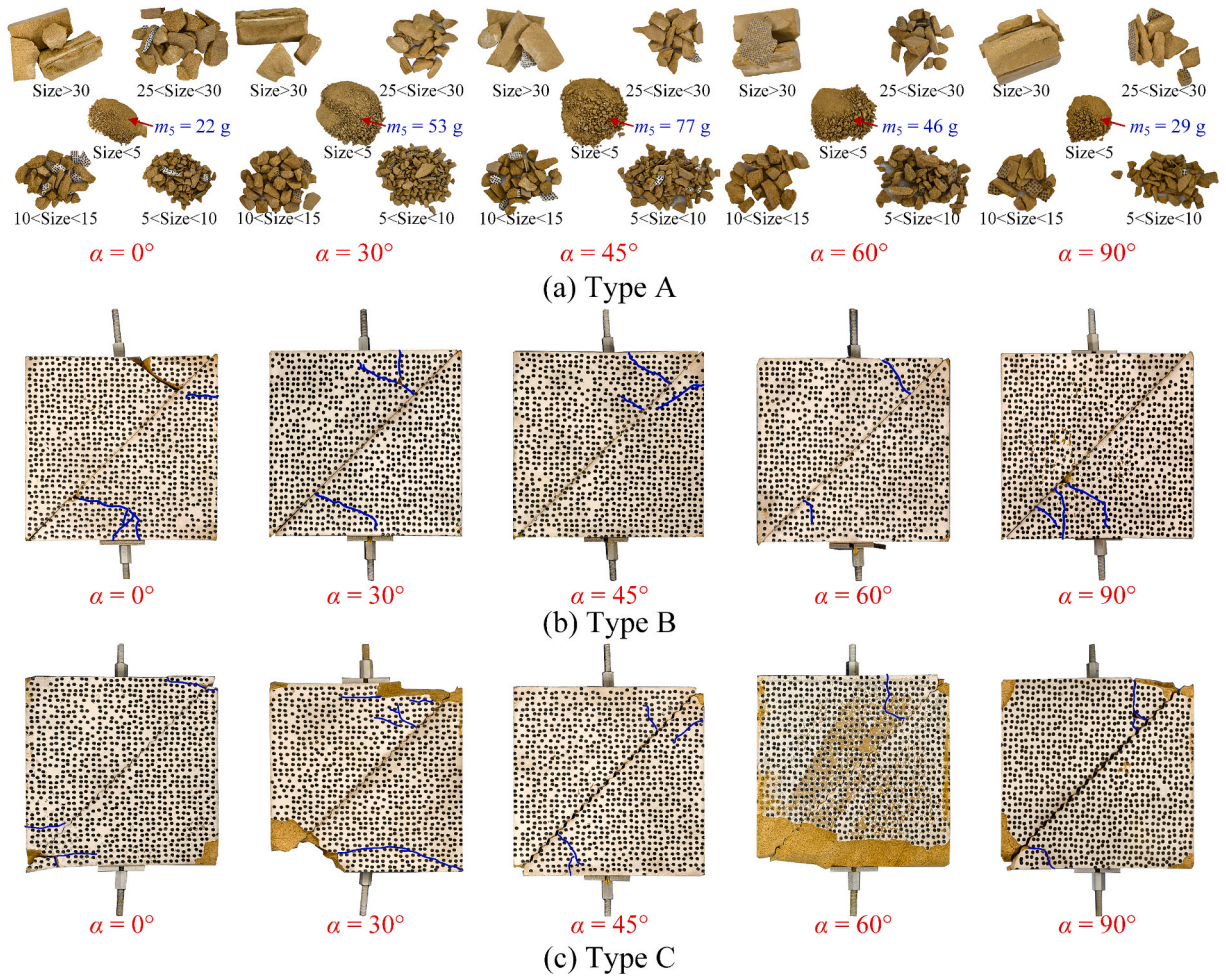



**Fig. 13.** Final failure patterns: (a) Type A; (b) Type B; (c) Type C.

continuously stored as elastic strain energy. Once the instability threshold is reached, the stored elastic energy is released abruptly over a short period, leading to more severe overall fragmentation. The degree of fragmentation is substantially greater than that observed in anchored units containing through-going structural planes. A sieve-based statistical analysis of post-failure fragments indicates that particle size distribution varies markedly with bedding dip angle. When the bedding dip angle is 45°, the fragment size distribution shifts toward finer particles (Fig. 13a). For example, for fragments smaller than 5 mm ($m_5$), the corresponding mass reaches 77 g at a bedding dip angle of 45°, which is substantially higher than the 22 g measured at a bedding dip angle of 0°. In contrast, in anchored units containing through-going structural planes, these planes are activated at an early stage of impact loading. Impact energy can therefore be rapidly released along through-going structural planes and effectively dissipated through relative displacement and sliding along the discontinuities. This mechanism reduces sustained accumulation of elastic strain energy within the specimen. As a result, overall fragmentation is comparatively lower. Secondary cracks can be observed propagating along bedding, connecting through-going structural planes with the primary crack in the anchorage zone, thereby forming the dominant failure path.

### *3.3. Analysis of the failure process of the surrounding rock in anchored units*

In summary, it is difficult to effectively analyze surrounding rock failure processes in anchored units solely from conventional high-speed camera images and final failure morphology. Digital image correlation (DIC), a non-contact optical measurement technique that derives displacement and strain fields from surface image variations during loading, has been widely applied in rock dynamics to support mechanism analysis [38,39]. Therefore, DIC was adopted in this work, and displacement and strain fields during impact loading were computed using the Ncorr program [40] implemented on the MATLAB platform.

Fig. 14 uses the anchored unit with a bedding dip angle of 0° as an example to illustrate the horizontal displacement field and maximum principal strain field during loading (time points marked "–" correspond to moments before peak load, whereas "+" corresponds to moments after peak load). Owing to the image acquisition rate, the captured frames cannot correspond exactly to the actual loading time; therefore, the images shown correspond to the closest recorded moments to the actual loading state, with a

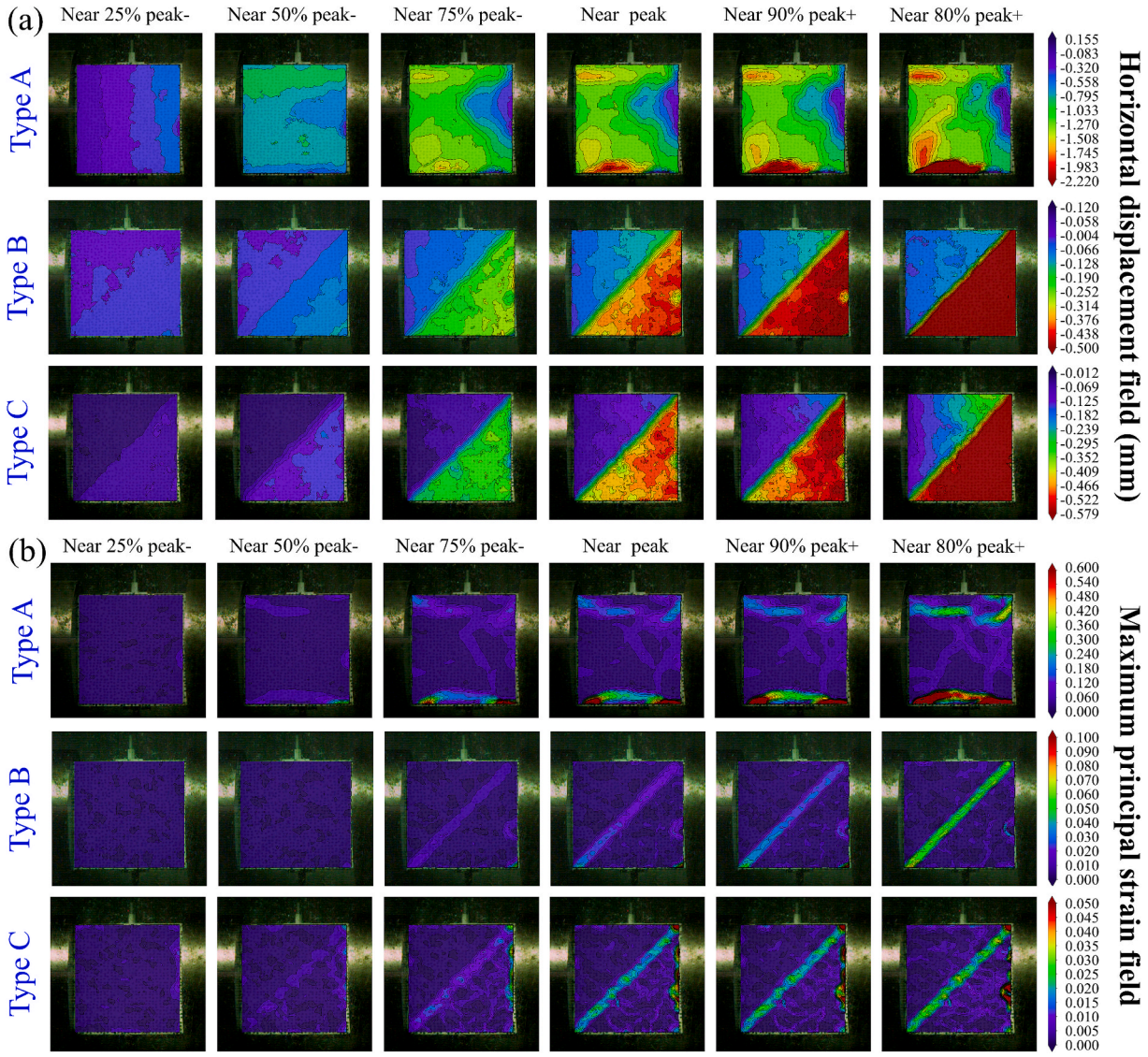



**Fig. 14.** Horizontal displacement field (a) and maximum principal strain field (b) at typical loading stages for a bedding dip angle of 0° (where the density of contour lines represents the gradient of variation).

maximum time deviation of 15 μs. Stress-wave propagation alters the motion tendency of constituent particles in the specimen, and the deformation field (displacement or strain) can reflect stress-wave propagation paths to some extent [41].

As shown in Fig. 14a, after entering the anchored unit from the right side, the stress-wave propagation path was deflected by structural surfaces (fracture surfaces and bedding planes). Ideally, in anchored units without fracture surfaces, the stress wave first propagates horizontally along the loading direction (near 25% peak–). When the wave reaches the specimen–transmitted bar interface, a reflected wave is generated and travels back into the specimen. The superposition of the forward-traveling and reflected waves promotes stress redistribution within the specimen [42]. In the presence of a smooth fracture surface, the stress wave undergoes pronounced deflection at the fracture surface, and wave velocity decreases after transmission across it. For example, at the near 75% peak– stage in Fig. 14a, the gradient of the horizontal displacement field ahead of the fracture surface is no longer horizontal but becomes perpendicular to the fracture surface; behind the fracture surface, the displacement-field gradient is nearly horizontal, and contour spacing is larger than that in the region ahead of the fracture surface.

For serrated fracture surfaces, stress-wave propagation is influenced by serration geometry, and wave deflection and superposition are preferentially distributed along the fracture-surface orientation; the displacement field near the fracture surface exhibits a serrated pattern. The loading characteristics of the anchored unit and disturbance-induced stress redistribution led to distinct deformation responses (Fig. 14b). The maximum principal strain field reflects crack initiation and propagation, and strain concentration zones in anchored units without fracture surfaces correspond closely to the observed crack distribution. Therefore, based on the maximum

principal strain field, deformation in anchored units containing fracture surfaces is inferred to be mainly concentrated near the fracture surface.

The above analysis mainly examined the influence of fracture surfaces on disturbance stress-wave propagation. Bedding also affects stress-wave propagation (Fig. 15). The specimen peak-load moment corresponds to the instant when the incident and reflected waves reach maximum superposition within the specimen; this state effectively reflects stress-wave superposition patterns inside the specimen. As shown in Fig. 15a, for anchored units without fracture surfaces, wave propagation at a bedding dip angle of 90° is closest to the initial propagation path of the incident wave. At other bedding dip angles, wave propagation either deflects at bedding interfaces or changes due to crack development along bedding. For specimens containing fracture surfaces, wave propagation at a bedding dip angle of 90° is also closest to the initial propagation path of the incident wave. The vertical bedding layers gradually reduce wave propagation velocity; for example, in Type C specimens with a bedding dip angle of 90°, horizontal displacement contours become increasingly sparse along the propagation direction. This observation partly explains why the loading rate of the anchored units is lowest at a bedding dip angle of 90° in Fig. 8d. From the maximum principal strain field, bedding exerts a significant influence on crack propagation in anchored units without fracture surfaces. In contrast, for specimens containing fracture surfaces, although visible cracks do not initiate, an obvious strain concentration develops along bedding interfaces (Fig. 15b).

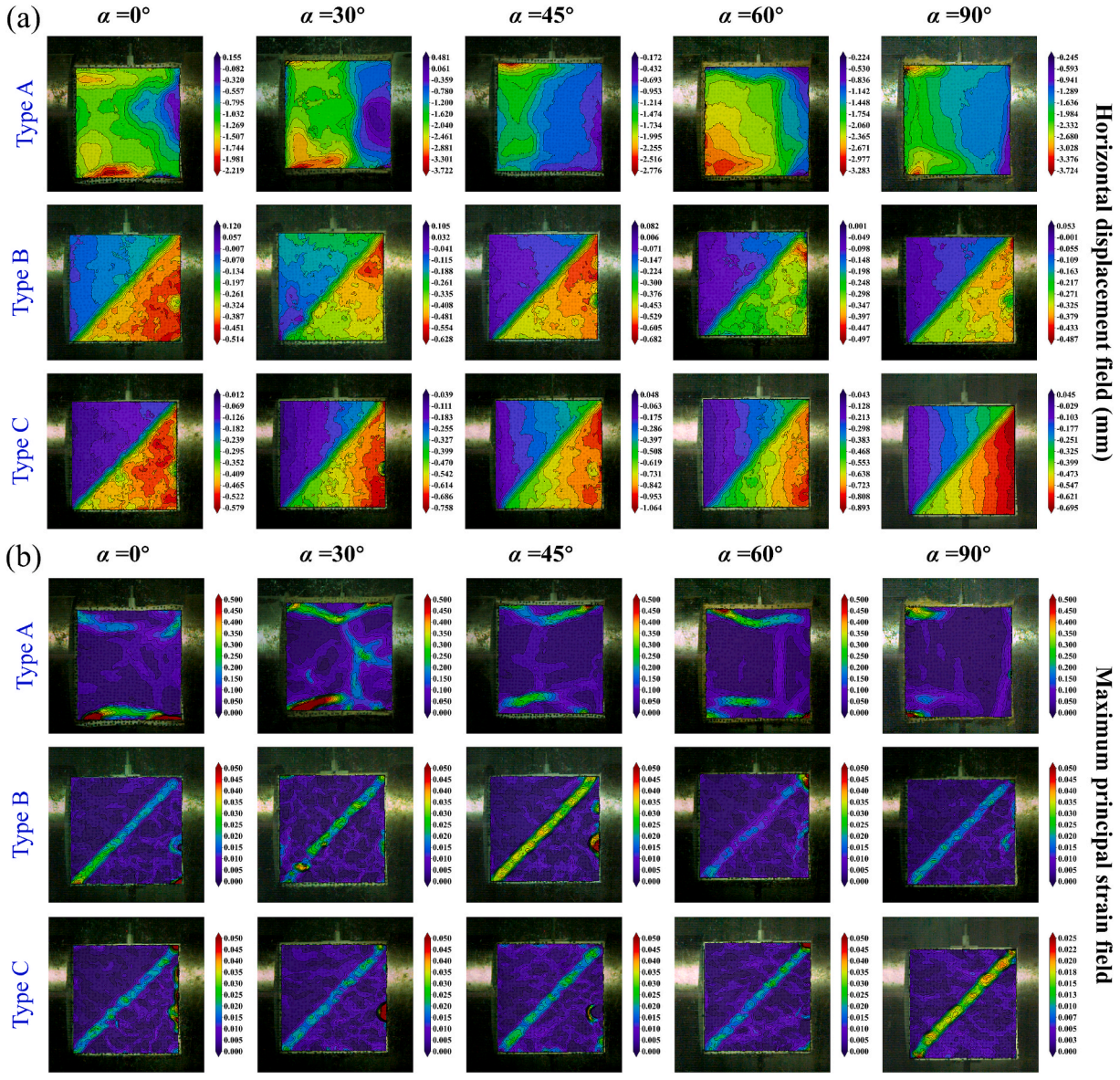



**Fig. 15.** Horizontal displacement field (a) and maximum principal strain field (b) at the peak-load state (where the density of contour lines represents the gradient of variation).

## 4. Numerical simulation based on FDM-DEM coupling

### 4.1. Establishment of the numerical model

Capturing detailed physical and mechanical responses of specimens under dynamic disturbance (e.g., crack propagation and the full-time evolution of bolt axial force) remains challenging in conventional laboratory testing. For example, resolving finer crack-propagation processes requires a higher-frame-rate high-speed camera, and the reliable measurement range of strain-gauge-based bolt axial-force monitoring is limited. Numerical simulation has therefore been widely used as a complementary approach [43]. In this work, a scaled SHPB testing system was constructed using a coupled finite difference–discrete element (FDM–DEM) framework to reproduce the response of the anchored units under dynamic disturbance (Fig. 16). The incident bar, transmitted bar, and bolt were modeled as continuum elements using the finite difference method, whereas the surrounding rock unit was modeled as particles using the discrete element method [44–46]. A shared-boundary scheme (the ball–wall–zone coupling method used in this work) was adopted: displacement or velocity from the continuum elements is applied as boundary conditions to the particles, and particle-generated forces are fed back to continuum nodes, thereby enabling two-way force–displacement exchange (Fig. 16a, b). Based on the mechanical characteristics of the modeled system and previous work [16,45–47], the linear parallel bond model was selected for contacts in the surrounding rock unit, the smooth-joint model was selected for contacts along closed fracture surfaces, and an elastic constitutive model was used for the bars and bolt. The component structures of the linear parallel bond and smooth-joint models are

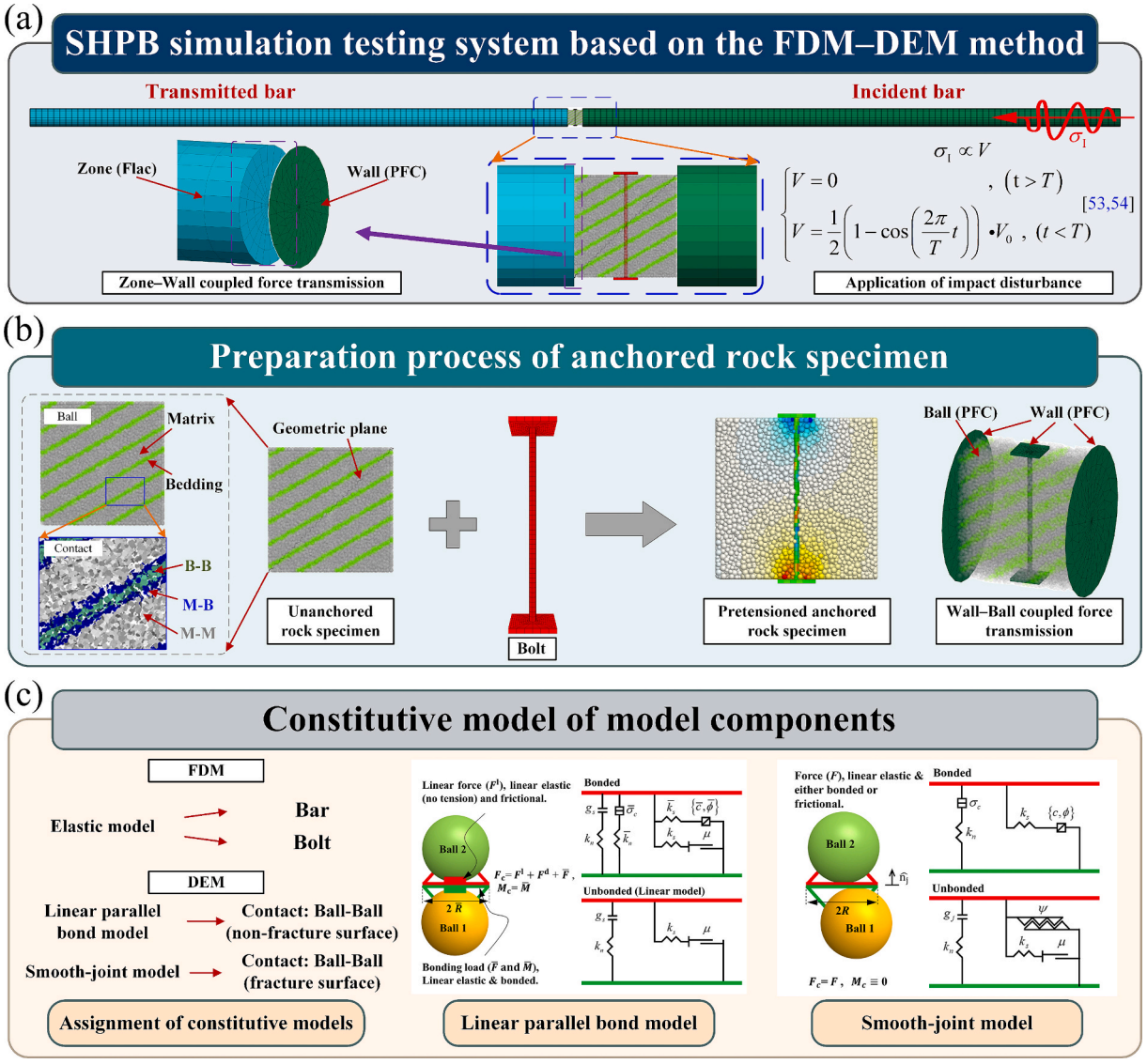



**Fig. 16.** SHPB testing system based on the coupled FDM–DEM method.

shown in Fig. 16c.

Two main approaches are commonly used in numerical simulations to introduce dynamic stress waves in an SHPB system: (i) wave generation via shaped striker impact [46,48,49] and (ii) stress-boundary loading [50–52]. For the shaped striker approach, wave period is difficult to control, and bar length must be adjusted to obtain a near half-sine stress wave [48]. Therefore, the stress-boundary loading method was adopted in this work. It should be noted that the experimentally measured incident-wave history was not directly applied in the numerical model. Instead, an idealized loading function with equivalent amplitude, duration, and dominant frequency characteristics was adopted to represent impact loading. This approach was employed to avoid potential numerical instability caused by noise and high-frequency fluctuations in the measured signals. Specifically, a periodic velocity [53,54] was applied to grid nodes of the continuum elements at the incident end of the incident bar, and the periodic function is given in Eq. (4).

$$\begin{cases} V = 0\ ,\ (t > T) \\ V = \dfrac{1}{2}\left(1 - \cos\left(\dfrac{2\pi}{T}t\right)\right) \cdot V_0\ ,\ (t < T) \end{cases} \tag{4}$$

where, $T$ is the period of the incident stress wave, $V$ is the velocity applied to the grid nodes and $V_0$ is the peak velocity. This method enables direct introduction of a half-sine stress wave with a prescribed period, and the peak value of the incident stress wave can be controlled by adjusting $V_0$. As shown in Fig. 17a, the peak of the incident stress wave increases with increasing $V_0$. After multiple trials, it was confirmed that when the maximum nodal velocity was set to $V_0 = 2.87$ m/s, the numerically introduced incident stress wave agreed well with that produced in laboratory tests with a projectile driven by an air pressure of 0.3 MPa (Fig. 17b). With bar boundaries defined as static boundaries, propagation of the incident, reflected, and transmitted waves in the bars was reproduced accurately (Fig. 17c).

It should be emphasized that the primary objective of the numerical model in this work was not to precisely reproduce the complete stress-wave propagation process within the Hopkinson bar system. Rather, the model was developed to analyze differences in energy evolution, stress redistribution, and failure mechanisms of anchored specimens under different structural plane conditions. Accordingly, during model construction, priority was given to calibrating the incident wave to ensure that the loading level and loading rate applied to the specimen were consistent with the experimental conditions. In addition, stress-wave propagation in the model was examined to verify compliance with the one-dimensional stress-wave assumption and the stress-uniformity assumption in the

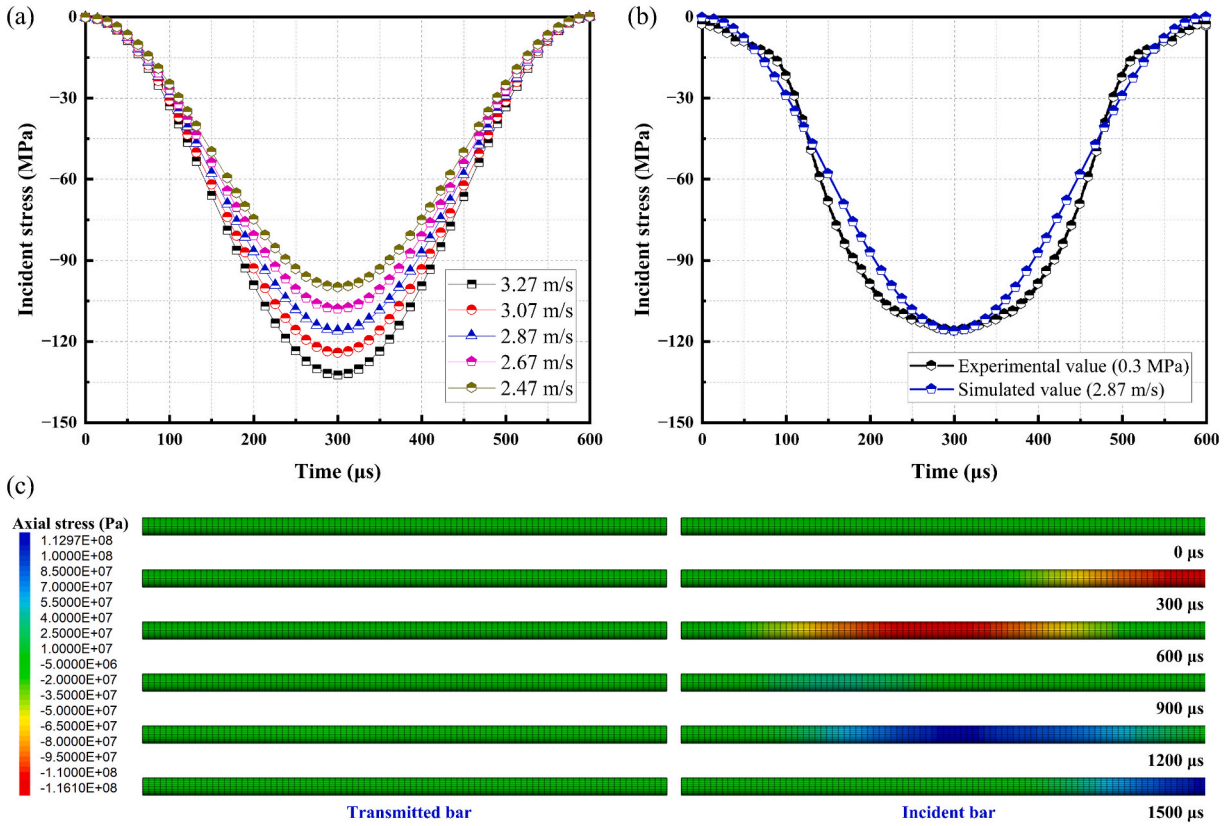



**Fig. 17.** Application of the stress wave: (a) incident stress-wave curves under different boundary velocities ($V_0$); (b) comparison between numerical and experimental incident stress waves; (c) evolution of incident stress-wave propagation in the bars (positive values: stress directed to the right; negative values: stress directed to the left).

specimen, thereby ensuring the applicability of wave-theory formulations and the three-wave method within the numerical framework. It should be noted that transmitted and reflected waves are influenced not only by specimen structural characteristics, but also by bar–specimen interface conditions and local non-one-dimensional effects. Such boundary-coupling effects are particularly pronounced in square specimens and in specimens containing through-going structural planes. Therefore, transmitted and reflected waves were not adopted as primary calibration targets in this work, but were instead used as qualitative reference indicators for comparison. Furthermore, model validity at the failure-pattern level was corroborated by comparing simulated failure morphology and dominant crack paths with those observed experimentally. A detailed description of model validation is provided in Section 4.2.

### 4.2. Validation of the numerical model

The one-dimensional stress-wave assumption and the stress-uniformity assumption are core requirements for correctly deriving dynamic mechanical properties using the SHPB system [55,56]. These assumptions require that the stress wave propagates along the bar axis, that only longitudinal waves participate in propagation, and that, after multiple reflections within the specimen, stresses at both specimen ends and within the specimen become uniform along the loading direction. To validate the reliability of the SHPB system constructed using the coupled FDM–DEM method, three groups of monitoring points were arranged along the bar axis near the bar–specimen interfaces. Group I consisted of points A and F, located 2,000 mm from the incident-bar–specimen interface and the transmitted-bar–specimen interface, respectively. Group II consisted of points B and E, located 1,500 mm from the two interfaces. Group III consisted of points C and D, located 1,000 mm from the two interfaces (Fig. 18a). Based on the evolution of axial and radial stresses at these monitoring points, the system satisfies the stress-uniformity assumption (axial stresses at different cross-sections of the same bar are nearly identical; Fig. 18b) and the one-dimensional stress-wave assumption (radial stress is sufficiently small relative to axial stress, indicating negligible radial dispersion; Fig. 18c).

After constructing the loading system, the anchored-unit specimen was discretized into particle assemblies using the particle-based parameters listed in Table 3. The specimen contact parameters were then calibrated using a trial-and-error procedure, and the final set of microscopic contact parameters is provided in Tables 4 and 5. A comparison between the dynamic mechanical responses of the calibrated numerical specimens and the corresponding laboratory results is presented in Fig. 19.

### 4.3. Energy dissipation analysis

During dynamic impact loading, part of the input energy is absorbed by the specimen and irreversibly dissipated. This dissipated energy reflects underlying failure mechanisms, including microcrack initiation, crack propagation, interfacial frictional slip, and

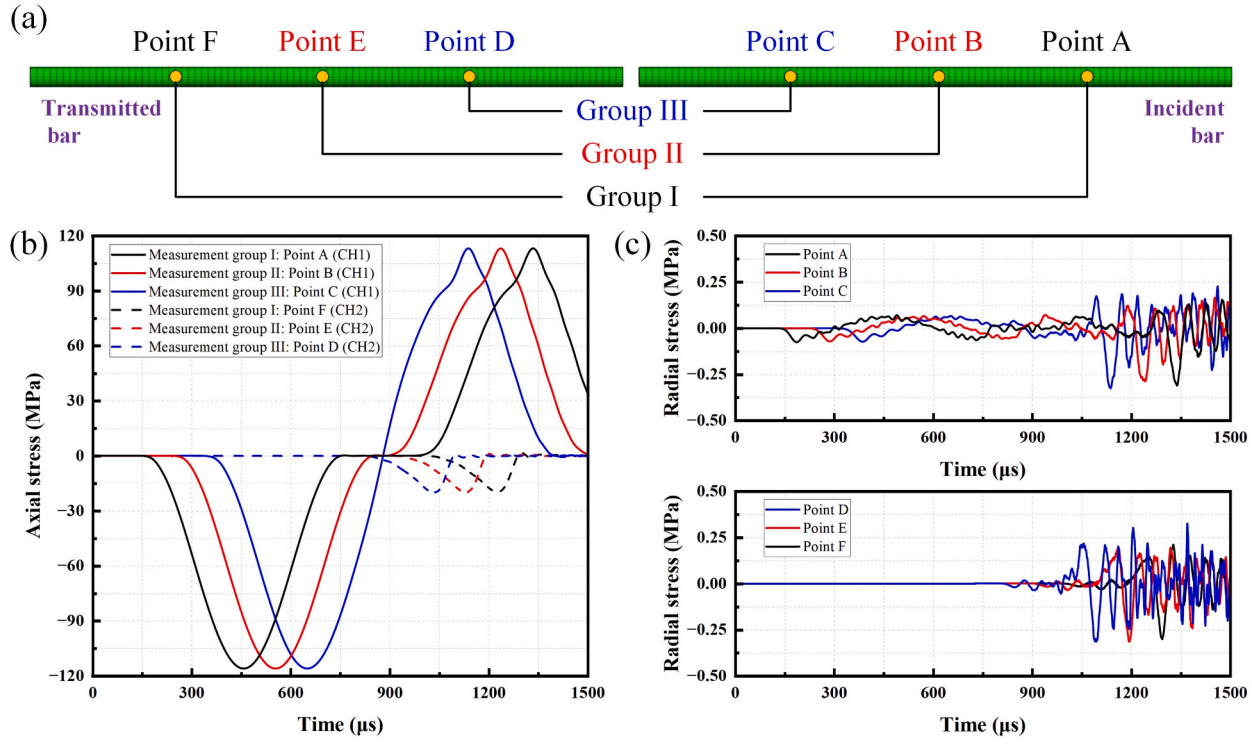



**Fig. 18.** Validation of the model reliability: (a) distribution of monitoring-point locations; (b) evolution of axial stress at the monitoring points; (c) evolution of radial stress at the monitoring points.

**Table 3**
Basic parameters of the particles.

| Parameter | Value |
|---|---|
| Particle size range (mm) | 0.8 ~ 1.3 |
| Particle density (kg/m$^3$) | 2299 |
| Effective elastic modulus (GPa) | 10 |
| Normal-to-shear stiffness ratio | 2.0 |
| Inter-particle friction coefficient | 0.5 |

**Table 4**
Microscopic contact parameters of the particles.

| Parameter | Contact groups | | |
|---|---|---|---|
| | Matrix–Matrix | Matrix–Bedding | Bedding–Bedding |
| Effective elastic modulus of parallel bonds (GPa) | 12.0 | 11.8 | 11.4 |
| Normal-to-shear stiffness ratio of parallel bonds | 2.0 | 2.0 | 2.0 |
| Normal bond strength of parallel bonds (MPa) | 148.5 | 105.2 | 96.5 |
| Shear bond strength of parallel bonds (MPa) | 62.0 | 58.6 | 53.7 |
| Inter-particle friction coefficient of parallel bonds | 0.5 | 0.5 | 0.5 |
| Friction angle (°) | 36.0 | 32.0 | 29.0 |

**Table 5**
Microscopic contact parameters of the smooth-joint constitutive model.

| Parameter | Value |
|---|---|
| Normal stiffness (GPa/m) | 1200 |
| Shear stiffness (GPa/m) | 1200 |
| Normal bond strength (MPa) | 0 |
| Shear bond strength (MPa) | 0 |
| Friction angle (°) | 30 |
| Friction coefficient | 0.2 |

material softening and damage [57–59]. Greater dissipated energy indicates stronger damage capacity and energy-absorption characteristics under dynamic loading. Compared with mechanical curves, energy analysis provides a more fundamental perspective for elucidating the influence of structural features (e.g., cracks and joint roughness) on rock dynamic failure behavior. However, conventional methods have difficulty quantifying the kinetic energy of fragments generated after specimen rupture. Although some researchers have attempted to estimate fragment kinetic energy using ultra-high-frame-rate high-speed cameras [60], accurate motion capture remains challenging, and the method is generally limited to relatively large fragments. Numerical simulation can quantify dissipation among different energy components during impact loading, while neglecting losses in the form of sound, light, and heat.

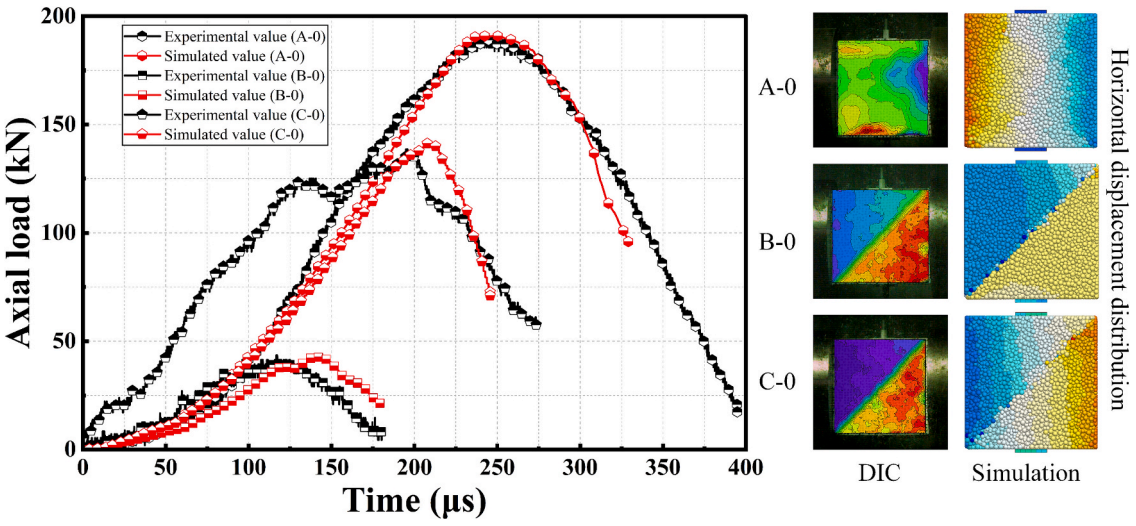



**Fig. 19.** Typical comparison between numerical simulation results and laboratory test results.

For the particle-assemblage surrounding rock used in this work, total energy ($U$) is mainly composed of elastic energy ($U_e$) and dissipated energy ($U_d$). Elastic energy ($U_e$) consists of particle strain energy (energy-strain, $E_a$) and bond strain energy (energy-bond, $E_b$). Dissipated energy ($U_d$) consists of kinetic energy (energy-kinetic, $E_k$), frictional slip energy (energy-slip, $E_s$) and damping energy (energy-damp, $E_d$) [61,62]. In this work, the contribution of damping energy is negligible and is therefore not discussed further.

Fig. 20a–c presents the evolution of key energy components in the surrounding rock during impact loading for three groups of anchored units with different fracture-surface characteristics at a bedding dip angle of 0°. Among elastic energy components ($U_e$), both particle strain energy ($E_a$) and bond strain energy ($E_b$) increased markedly with increasing load and decreased as the load attenuated. For the main dissipated energy components, kinetic energy ($E_k$) and frictional slip energy ($E_s$) increased continuously throughout impact loading. The influence of structural surfaces on surrounding-rock dissipated energy is dominated by fracture surfaces (Fig. 20d). Surrounding-rock dissipated energy was higher in anchored units without fracture surfaces than in those containing fracture surfaces, and it was higher for serrated fracture surfaces than for linear fracture surfaces. For example, at a bedding dip angle of 90°, surrounding-rock dissipated energy was 12.15 J for anchored units without fracture surfaces, 6.93 J for those with serrated fracture surfaces, and 4.00 J for those with linear fracture surfaces. Bedding effects on surrounding-rock dissipated energy were most pronounced in anchored units without fracture surfaces and least pronounced in those with linear fracture surfaces.

Furthermore, Fig. 21 shows how key energy components in the surrounding rock vary with bedding dip angle in the anchored units. Overall, the surrounding rock without fracture surfaces exhibited higher values for all key energy components than surrounding rock containing fracture surfaces, and surrounding rock with linear fracture surfaces had the lowest values. Among these energy components, bedding effects were more pronounced for dissipated energy than for elastic energy. For surrounding rock containing fracture surfaces, both $E_k$ and $E_s$ increased first and then decreased with increasing bedding dip angle, although the overall amplitude of variation was small. For surrounding rock without fracture surfaces, $E_k$ and $E_s$ increased first, then decreased, and finally increased again with bedding dip angle, and the overall amplitude of variation was relatively large. Regarding elastic energy, the ability of surrounding rock with linear fracture surfaces to store elastic energy was very limited, and all elastic energy components were substantially smaller than those of surrounding rock with the other two fracture-surface characteristics. This indicates that the stability of the surrounding-rock structure governs elastic energy storage capacity, which helps explain why rockbursts tend to occur in intact, hard, and brittle surrounding rock, whereas they are less likely in fragmented rock masses [63].

### 4.4. Analysis of force-chain contact characteristics

The three-dimensional contact fabric in PFC reflects force-chain structure (major load-bearing paths formed by a subset of strong contacts) by statistically analyzing distributions of contact numbers and contact forces, thereby revealing microstructural evolution during loading [64,65]. The distribution of contact numbers reflects the geometric arrangement of the particle skeleton, whereas contact forces represent principal load-bearing directions. Fig. 22 shows distributions of contact numbers and contact forces in the force-chain network of the anchored units at peak load. For anchored units without fracture surfaces, under axial impact loading, strong force chains are mainly aligned with the loading direction, and maximum contact forces are likewise concentrated along the

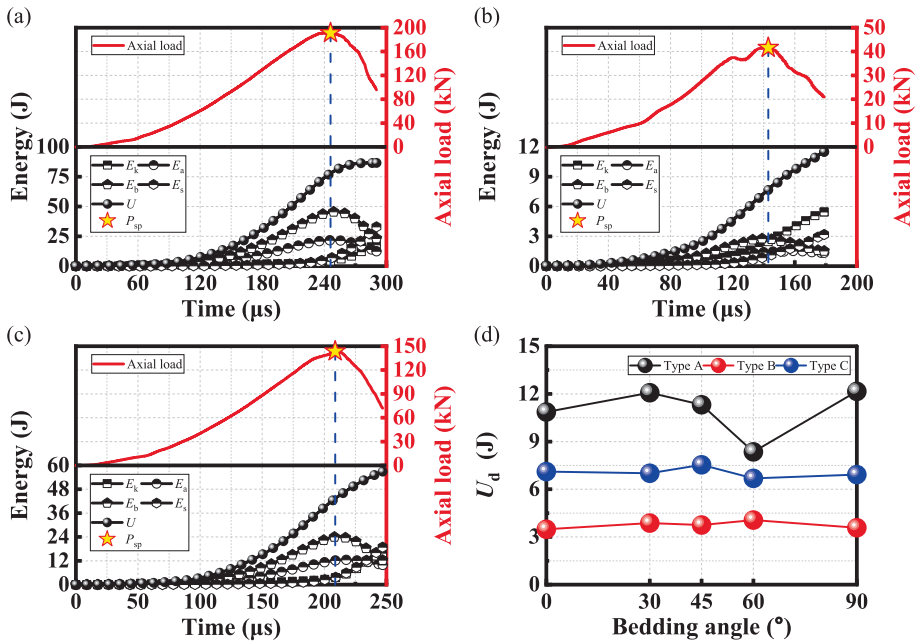



**Fig. 20.** Evolution of key energy components: (a) Type A; (b) Type B; (c) Type C; (d) variation of dissipated energy of the surrounding rock with bedding dip angle.

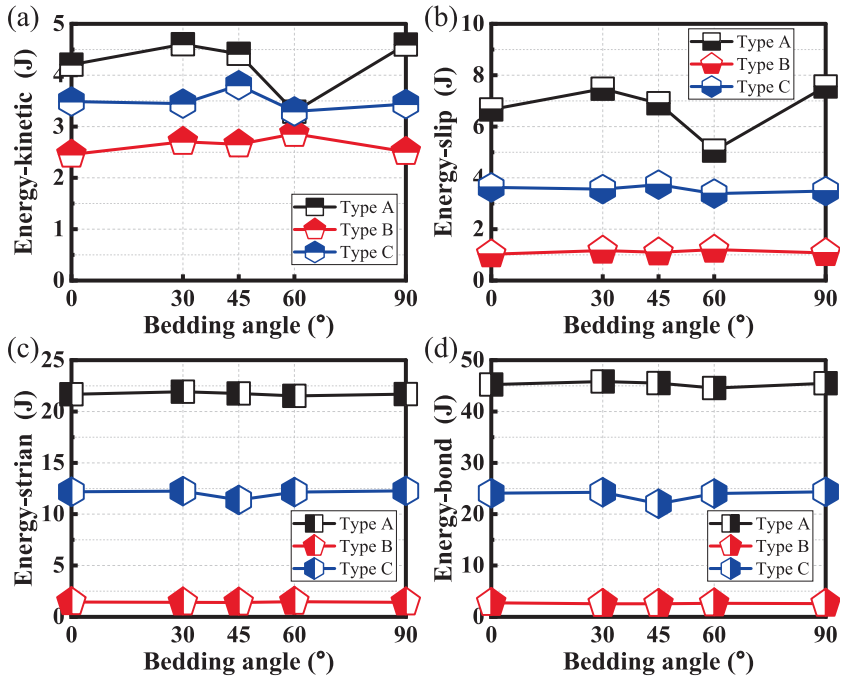



**Fig. 21.** Variation of key energy components with bedding dip angle: (a) energy-kinetic; (b) energy-slip; (c) energy-strain; (d) energy-bond.

loading direction. Fracture surfaces reorganize the force-chain network, causing force chains to reorient perpendicular to the fracture surface. Compared with serrated fracture surfaces, where interfacial mechanical interlocking is active, linear fracture surfaces induce a more concentrated clustering of contact forces. In terms of contact-force magnitude, specimens without fracture surfaces exhibit higher contact forces than those with fracture surfaces, and specimens with linear fracture surfaces exhibit the lowest contact-force levels. Among anchored units with different bedding dip angles, force-chain distributions show some differences, although these differences are smaller than those induced by fracture surfaces.

## 5. Discussion

### 5.1. Analysis of rock-bolt failure mechanisms

Five characteristic loading stages were selected to analyze bolt deformation (A: 50%$P_{sp}$–; B: 75%$P_{sp}$–; C: $P_{sp}$; D: 75%$P_{sp}$+; E: 50% $P_{sp}$ + ), as shown in Fig. 23. For anchored units without fracture surfaces, clear axial stress concentration occurs in the bolt at stage C. At stage D, axial stress increases markedly along the entire bolt, with prominent stress concentration at the bolt–tray interface. In addition, the entire bolt deforms toward the dynamic loading direction. Unlike anchored units without fracture surfaces, bolt failure in anchored units containing linear fracture surfaces is dominated by localized shear. At the fracture-surface intersection, the bolt exhibits pronounced bending, whereas axial stress concentration occurs only at the bending location. The increase in axial force in other parts of the bolt is relatively small, indicating that bolt axial restraint capacity is not fully mobilized. For anchored units containing serrated fracture surfaces, the bolt also exhibits noticeable bending at the fracture-surface intersection; however, axial stress increases along the bolt more generally, such that, except near the bending region, bolt axial force is relatively uniform and axial restraint capacity is partially mobilized.

In summary, for anchored units without fracture surfaces, bolt failure is dominated by overall tensile deformation, with potential failure regions located at the bolt midsection and the bolt–tray interface. For anchored units with linear fracture surfaces, bolt failure is dominated by localized shear deformation, with the potential failure region located at the fracture-surface intersection. For anchored units with serrated fracture surfaces, bolt failure is characterized by combined tensile–shear deformation, with potential failure regions located at the bolt midsection and the fracture-surface intersection. These findings are generally consistent with overall trends in bolt failure characteristics reported in previous laboratory investigations [3,66–68]. They also provide a plausible explanation for different load distribution patterns and failure phenomena of rock bolts reported in field monitoring studies [69–71]. These results further indicate that the morphology and spatial distribution of structural planes in the surrounding rock exert strong control over rock-bolt load transfer paths and failure modes.

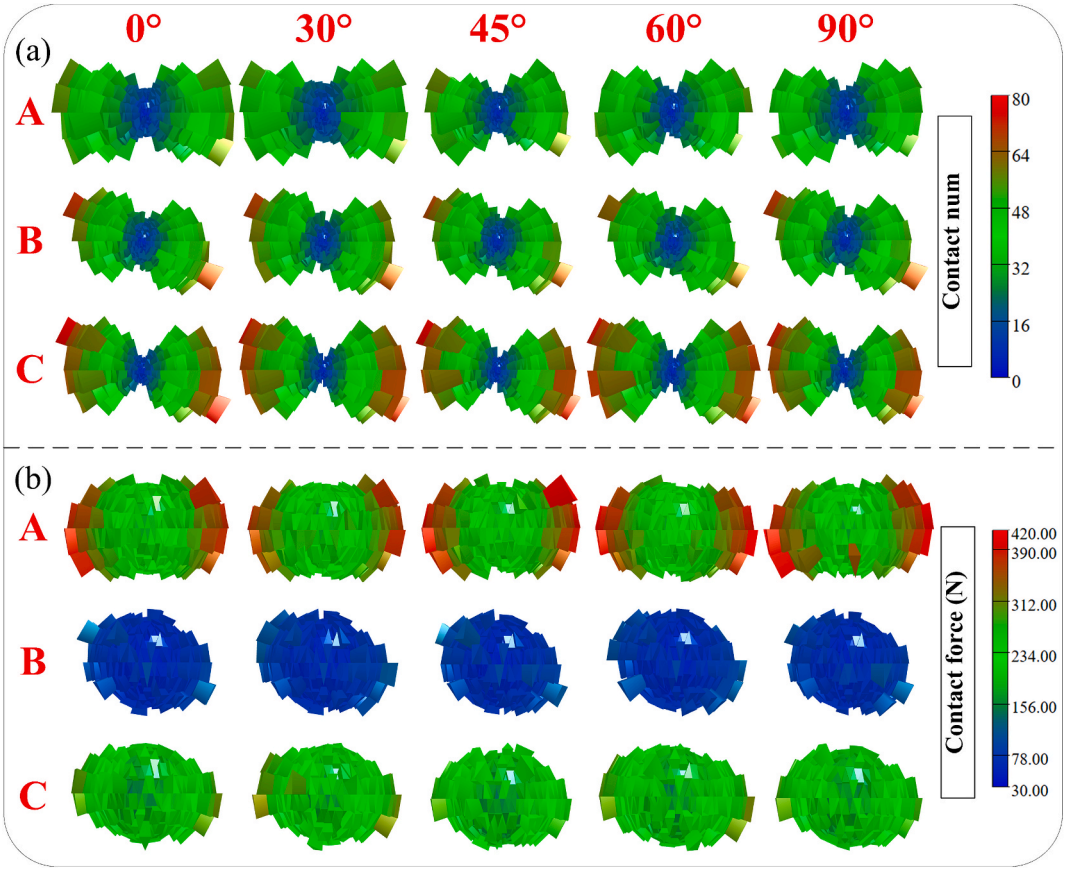



**Fig. 22.** Three-dimensional fabric analysis of the force-chain network at the peak-load time: (a) contact-number distribution; (b) contact-force distribution (where the major axis orientation represents the principal contact structural direction).

### *5.2. Analysis of failure mechanisms of the anchored surrounding rock*

Fig. 24a shows crack-density contours of the anchored units at 75% of the post-peak load ($t_{0.75P+}$). Notably, in anchored units without fracture surfaces, crack development exhibits clear directionality and propagates mainly vertically, tending to align with the loading direction. For anchored units containing fracture surfaces, internal crack development becomes more dispersed; in particular, in anchored units with linear fracture surfaces, the dominant crack-propagation direction also changes. Combined with particle displacement trends in Fig. 24b, it is evident—consistent with the analysis of Fig. 14 in Section 3.3—that fracture surfaces alter stress-wave propagation within the specimens. For specimens without fracture surfaces, stress waves propagate horizontally. The left side of the specimen exhibits end-face failure dominated by inertial effects, whereas the incident stress wave, after reflection at the specimen–transmitted bar interface, superimposes with the forward-traveling wave and generates tensile stress differences on the right side of the specimen, promoting vertical crack development (Fig. 15b). For anchored units with smooth fracture surfaces, relative particle motion occurs primarily along the smooth fracture surface, and structural stability is mainly governed by bolt anti-slip resistance. The stress wave undergoes significant deflection at the fracture surface; particle motion on the left side of the specimen becomes nearly perpendicular to the fracture surface. After transmission across the fracture surface, the reflected wave is also deflected, and the combined action of the deflected reflected wave and the forward wave produces a downward-left motion trend on the right side of the specimen. For serrated fracture surfaces, interlocking between serrations weakens stress-wave deflection. Consequently, particle motion on both sides of the fracture surface remains primarily horizontal. Thus, in Fig. 15a, the gradient direction of horizontal displacement contours for specimens with serrated fracture surfaces remains nearly horizontal.

In summary, anchored units without fracture surfaces exhibited the strongest bolt-anchoring performance. Their anchorage stress field, together with tensile stresses generated by reflected stress waves, promotes failure modes dominated by end-face failure on the anchoring side and vertical tensile cracking. Anchored units with fracture surfaces exhibited the weakest anchoring performance; the bolt primarily provides anti-slip resistance, and failure under dynamic disturbance occurs mainly through sliding along the fracture surface. For anchored units with serrated fracture surfaces, enhanced interlocking between serrations improves the overall integrity of surrounding rock containing fracture surfaces. Bolt failure occurs mainly through combined tensile–shear deformation, and stress-wave deflection is weakened, leading to failure concentrated within interlocking serration regions.

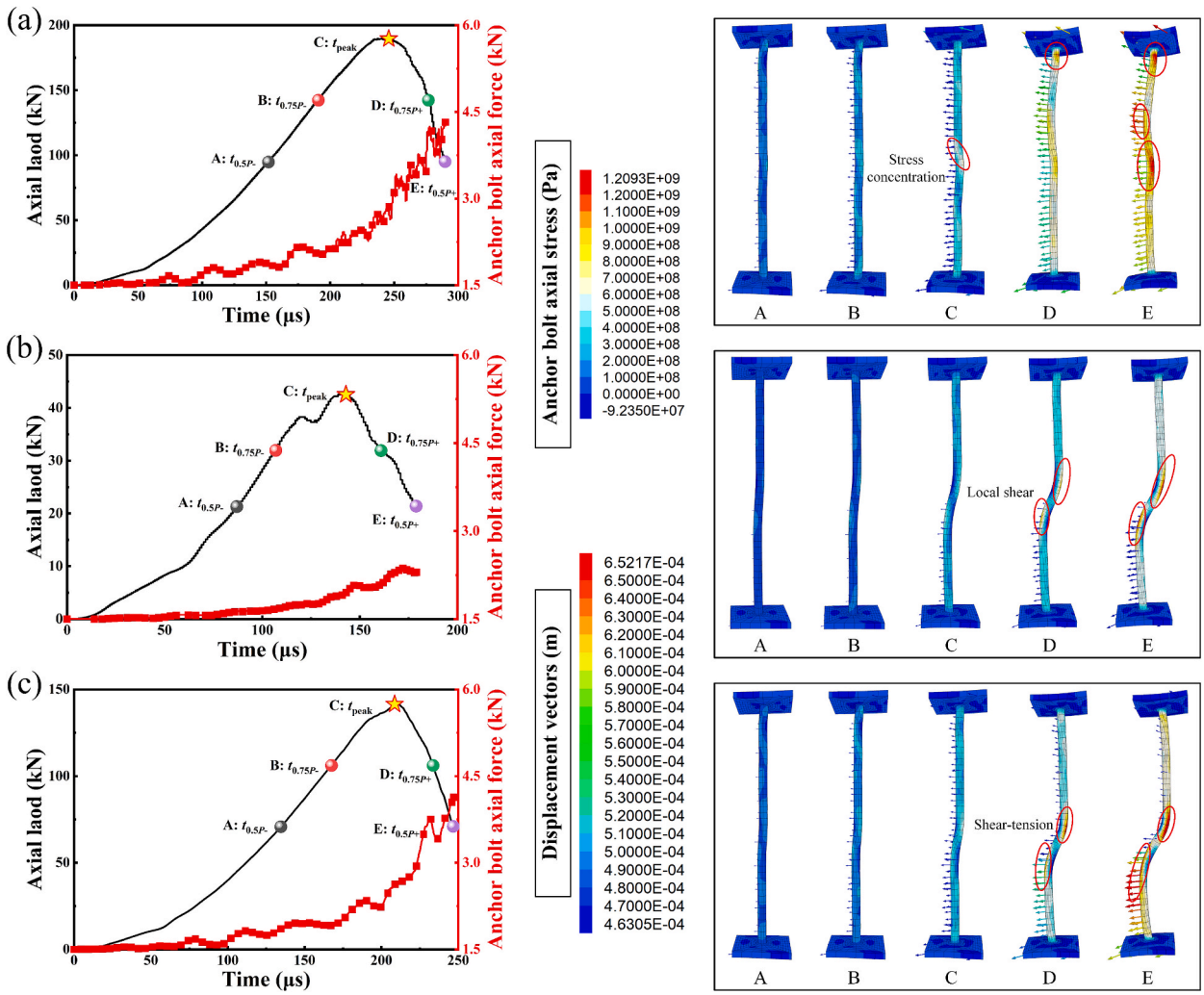



**Fig. 23.** Evolution of rock-bolt failure in anchored units with a bedding dip angle of 0°: (a) Type A; (b) Type B; (c) Type C (bolt deformation in the plotted images magnified by a factor of 20 to highlight small deformations).

## 6. Engineering implications and limitations

### *6.1. Engineering implications*

The results indicate that the through-going characteristics of structural planes significantly influence impact-energy transmission paths and bolt-force evolution under dynamic loading. In surrounding rock masses containing linear through-going structural planes, rock bolts are more likely to assume a tangential restraint role during dynamic disturbance, and axial force exhibits a sustained increasing trend. In such cases, support design should prioritize improving bolt shear resistance and coordinated deformation capacity. In contrast, under conditions without through-going structural planes or with serrated through-going structural planes, bolt axial force shows a pronounced unloading stage after reaching its peak, highlighting the importance of axial load-bearing capacity and energy dissipation capability. Moreover, through-going structural planes can dissipate impact energy at an early stage and alter surrounding rock failure modes. In engineering practice, zoning control strategies may therefore be implemented based on the degree of structural plane connectivity. In regions prone to significant relative displacement, particular attention should be paid to preventing rock-bolt shear and sliding failure. In more intact regions where elastic strain energy tends to accumulate, the risk of sudden brittle failure should be carefully considered. In addition, distinct axial force–time evolution patterns under different structural conditions provide a basis for monitoring and early warning. A continuously increasing axial force does not necessarily indicate global instability, whereas a rapid peak followed by unloading may signal the risk of concentrated energy release. These findings can be used to optimize threshold settings for bolt monitoring systems, thereby improving the safety and specificity of support design and operational management under dynamic loading without requiring modifications to existing construction or monitoring frameworks.

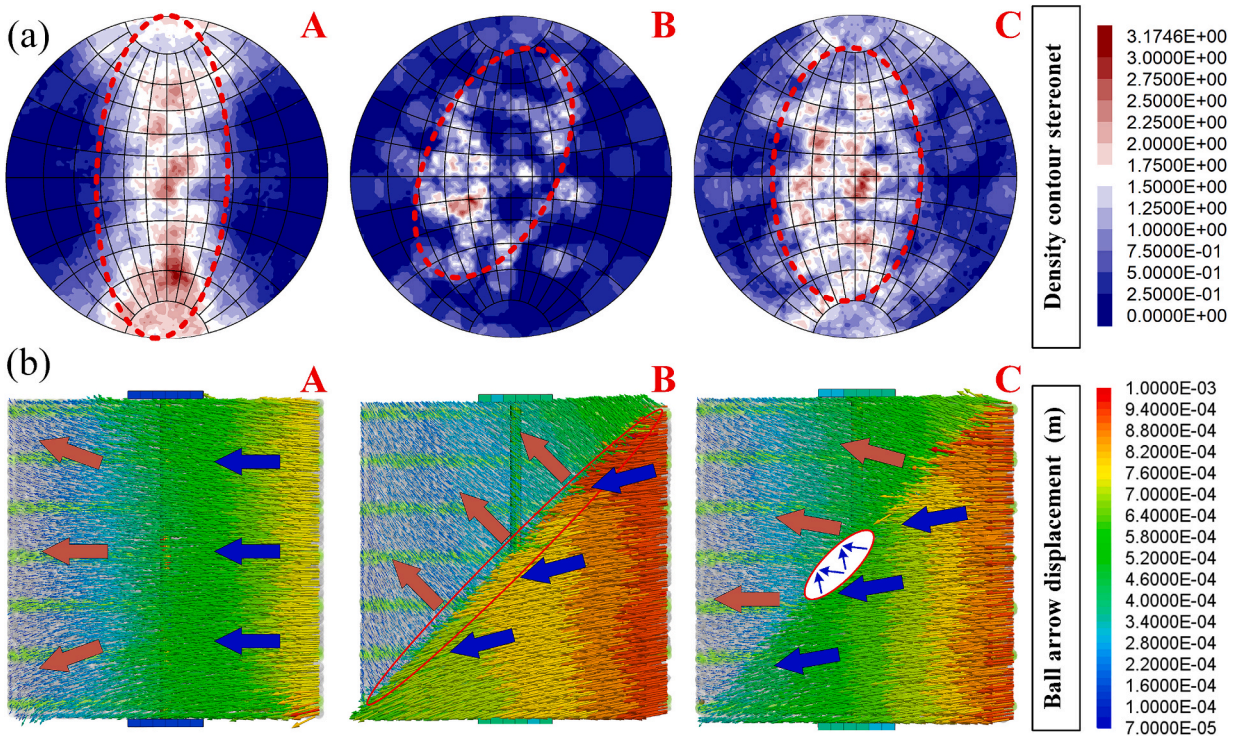



**Fig. 24.** Anchored units at 75% of the post-peak load: (a) crack distribution; (b) particle displacement trends (bedding dip angle of 0°).

### *6.2. Limitations*

This work involves several simplifications in experimental modeling and parameter selection; therefore, the scope of applicability of the conclusions should be clearly defined. (1) Due to experimental constraints, a geometric similarity ratio of 1:10 was adopted for scaled modeling. The corresponding results are intended to elucidate relative dynamic response characteristics and instability evolution mechanisms of anchored surrounding rock under different structural plane conditions, rather than to provide direct quantitative predictions at full engineering scale. (2) A single impact energy level was applied in this work. The analysis focused on comparative dynamic response patterns of the anchorage system under varying structural plane conditions. Consequently, the conclusions mainly reflect response characteristics under a specific impact intensity. (3) In the dynamic analysis, the bolt material was characterized using a static elastic modulus, and strain-rate dependence was not explicitly incorporated. Although this simplifying assumption may affect the absolute magnitude of bolt peak axial force, it does not alter the comparative conclusions regarding bolt-force evolution trends and associated failure modes under different structural plane conditions.

## 7. Conclusions

In this work, dynamic impact tests were performed on anchored units with complex geological features, including different bedding dip angles and fracture-surface characteristics. Using digital image correlation (DIC) and numerical simulations based on a coupled finite difference–discrete element method, this work examined the effects of bedding dip angle and fracture surfaces on the dynamic mechanical response of the anchored units. In addition, this work discusses stress-wave propagation paths and dynamic failure mechanisms of the anchored units under different fracture-surface characteristics. The main conclusions are as follows.

(1) Fracture surfaces significantly reduced the loading rate, peak load, and dissipated energy of the anchored units, and the magnitude of these reductions was negatively correlated with fracture-surface roughness. The linear fracture surface ($JRC = 0$) yielded the lowest loading rate (only approximately 28% of that of specimens without fracture surfaces), with a peak load of 42.8 kN and a surrounding-rock dissipated energy of approximately 4.0 J. The serrated fracture surface ($JRC = 16$) resulted in higher loading rate and dissipated energy than the linear fracture surface, with a peak load of 141.6 kN, and exhibited multi-peak characteristics.
(2) Bedding dip angle plays a regulatory role in the mechanical response of the anchored units, although its overall influence is weaker than that of fracture surfaces. For specimens without fracture surfaces, peak load increased first, then decreased, and finally recovered slightly with increasing bedding dip angle, with the highest bearing capacity occurring at 30°. For specimens

with linear fracture surfaces, loading rate varied by up to 59.97%, and peak load decreased first and then increased. Bedding effects were smallest for serrated fracture surfaces, although local effects could still guide crack-propagation direction.

(3) The combined effects of fracture surfaces and bedding altered stress-wave propagation paths and local strain distributions. Without fracture surfaces, stress waves propagated along the loading direction and promoted end-face tensile failure. wave velocity, resulting in cracks propagating along the fracture surface. Linear fracture surfaces caused wave deflection and reduced wave velocity, resulting in cracks propagating along the fracture surface. Serrated fracture surfaces weakened wave deflection, and failure concentrated within interlocking serration regions. Bedding dip angle affected crack-propagation direction by modulating wave velocity and reflection paths.

(4) Failure modes of the bolt and anchored surrounding rock are mainly governed by fracture-surface characteristics. Without fracture surfaces, the bolt failed primarily through overall tensile deformation and exhibited the highest confinement capacity. With linear fracture surfaces, localized shear failure dominated, and the potential failure region was concentrated at the fracture-surface intersection. With serrated fracture surfaces, failure occurred through combined tensile–shear mechanisms, bolt axial force was more uniformly distributed, and interlocking between serrations enhanced surrounding rock integrity. Bedding primarily regulated the spatial distribution of failure and crack-propagation direction.

## CRediT authorship contribution statement

**Xiaofeng Qin:** Writing – review & editing, Writing – original draft, Visualization, Project administration, Methodology, Investigation, Funding acquisition, Formal analysis, Data curation, Conceptualization. **Haijian Su:** Writing – review & editing, Project administration, Methodology, Funding acquisition, Conceptualization. **Liyuan Yu:** Supervision, Resources, Investigation, Funding acquisition. **Thi Nhan Pham:** Resources, Investigation, Data curation. **Wei Li:** Resources, Investigation, Data curation. **Bowen Hu:** Validation, Data curation.

## Declaration of competing interest

The authors declare that they have no known competing financial interests or personal relationships that could have appeared to influence the work reported in this paper.

## Acknowledgements

**Funds:** This work was financed by the National Natural Science Foundation of China (Grant Nos. 52274100 and U24B2040), the Fundamental Research Funds for the Central Universities (Grant No. 2025-00050), the Postgraduate Research & Practice Innovation Program of Jiangsu Province (Grant No. KYCX25_2901), and the Graduate Innovation Program of China University of Mining and Technology (Grant No. 2025WLKXJ220). These supports are gratefully acknowledged.

## Data availability

Data will be made available on request.

## References

[1] M. He, S. Ren, H. Xu, S. Luo, Z. Tao, C. Zhu, Experimental study on the shear performance of quasi-NPR steel bolted rock joints, J. Rock Mech. Geotech. Eng. 15 (2023) 350–362, https://doi.org/10.1016/j.jrmge.2022.03.011.

[2] Q. Sui, M. He, P. He, M. Xia, Z. Tao, State of the art review of the large deformation rock bolts, Undergr. Space 7 (2022) 465–482, https://doi.org/10.1016/j.undsp.2021.11.001.

[3] Y. Chen, H. Xiao, State-of-the-art on the anchorage performance of rock bolts subjected to shear load, Int. J. Coal Sci. Technol. 11 (2024) 9, https://doi.org/10.1007/s40789-023-00643-z.

[4] H. Kang, P. Jiang, Y. Wu, F. Gao, A combined "ground support-rock modification-destressing" strategy for 1000-m deep roadways in extreme squeezing ground condition, Int. J. Rock Mech. Min. Sci. 142 (2021) 104746, https://doi.org/10.1016/j.ijrmms.2021.104746.

[5] F. He, G. Li, V. Carvelli, X. Xu, X. Feng, J. Kan, Rock bolts under cyclic loading: Mechanical performance and damage assessment by acoustic emissions, Eng. Fail. Anal. 157 (2024) 107940, https://doi.org/10.1016/j.engfailanal.2023.107940.

[6] X. Wu, H. Zheng, Y. Jiang, T. Deng, G. Xiao, Y. Wang, Effect of cyclic shear loading on shear performance of rock bolt under different joint roughness, Rock Mech. Rock Eng. 56 (2022) 1969–1980, https://doi.org/10.1007/s00603-022-03174-2.

[7] X. Sun, L. Wang, L. Cui, Y. Zhang, M. Jiang, Experimental investigation of biaxial compressive mechanical property of NPR anchored rock with different preload forces, Tunn. Undergr. Space Technol. 146 (2024) 105621, https://doi.org/10.1016/j.tust.2024.105621.

[8] K. Wang, J. Yang, W. Bian, Y. Wu, Z. Sun, Y. Fang, Dynamic behavior of anchorage systems reinforced with high-performance npr bolts: Laboratory and field investigation, Constr. Build. Mater. (2025), https://doi.org/10.2139/ssrn.5194706.

[9] S. Khaleghparast, N. Aziz, A. Remennikov, S. Anzanpour, An experimental study on shear behaviour of fully grouted rock bolt under static and dynamic loading conditions, Tunn. Undergr. Space Technol. 132 (2023) 104915, https://doi.org/10.1016/j.tust.2022.104915.

[10] B. Jiang, K. Wu, Q. Wang, Y. Wang, W. Wu, Y. Feng, Y. Zhang, Dynamic damage characteristics and control mechanism of rocks anchored by constant resistance and energy absorption material, Int. J. Min. Sci. Technol. 35 (2025) 57–67, https://doi.org/10.1016/j.ijmst.2024.12.005.

[11] X. Wu, L. Jiang, M. Tao, S. Mitri Hani, G. Xiang, Dynamic behaviors and bolt-strengthening effect of sand-powder 3D printing rock analog under static and dynamic coupled loading, Constr. Build. Mater. 411 (2024) 134723, https://doi.org/10.1016/j.conbuildmat.2023.134723.

[12] P. Wang, N. Zhang, Q. Wei, X. Xu, G. Cui, A. Li, S. Yang, J. Kan, Mechanical responses of anchoring structure under triaxial cyclic loading, J. Rock Mech. Geotech. Eng. 16 (2024) 545–560, https://doi.org/10.1016/j.jrmge.2023.04.020.

[13] D. Fan, X. Liu, Y. Tan, X. Li, S. Yang, Energy mechanism of bolt supporting effect to fissured rock under static and dynamic loads in deep coal mines, Int. J. Min. Sci. Technol. 34 (2024) 371–384, https://doi.org/10.1016/j.ijmst.2024.03.001.

[14] Q. Wang, W. Wu, Y. Wang, M. He, H. Xue, H. Wei, Evolution and control mechanism of rockburst in rock anchored by new energy-absorbing material, Rock Mech. Rock Eng. 56 (2023) 4569–4582, https://doi.org/10.1007/s00603-023-03260-z.
[15] X. Xin, Q. Meng, X. Zhang, Fracture mechanism and energy dissipation characteristics of coal-rock composite anchored body with through-going joints, Int. J. Numer. Anal. Methods Geomech. (2026), https://doi.org/10.1002/nag.70264.
[16] Y. Chen, D. Yu, Y. Wang, Y. Zhao, H. Yang, L. Huang, Dynamic characteristics and anchorage mechanisms of fractured granite: Analytical, numerical and experimental analyses, Rock Mech. Rock Eng. (2024), https://doi.org/10.1007/s00603-024-04249-y.
[17] W. Li, X. Li, Y. Mei, G. Wang, W. Yang, H. Wang, A numerical simulation approach of energy-absorbing anchor bolts for rock engineering, Int. J. Rock Mech. Min. Sci. 158 (2022) 105188, https://doi.org/10.1016/j.ijrmms.2022.105188.
[18] Y. Chen, Z. Deng, L. Huang, H. Lin, Y. Wang, Y. Liang, C. Lin, Anchoring mechanism of tunnel free face subjected to dynamic–static combined load, Rock Mech. Rock Eng. (2026), https://doi.org/10.1007/s00603-026-05285-6.
[19] X. Feng, B. Gong, Z. Liang, S. Wang, C. Tang, H. Li, T. Ma, Study of the dynamic failure characteristics of anisotropic shales under impact Brazilian splitting, Rock Mech. Rock Eng. 57 (2023) 2213–2230, https://doi.org/10.1007/s00603-023-03673-w.
[20] W. Wang, Y. Zhao, Z. Sun, C. Lu, Effects of bedding planes on the fracture characteristics of coal under dynamic loading, Eng. Fract. Mech. 250 (2021) 107761, https://doi.org/10.1016/j. engfracmech.2021.107761.
[21] X. Chang, X. Zhang, L.Z. Qian, S.H. Chen, J. Yu, Influence of bedding anisotropy on the dynamic fracture behavior of layered phyllite, Eng. Fract. Mech. 260 (2022) 108183, https://doi.org/10.1016/j.engfracmech.2021.108183.
[22] J. Li, C. Wang, F. Ren, C. Wang, H. Li, Effect of bedding angle on mechanical properties of anchored shale, Rock Mech. Rock Eng. (2025), https://doi.org/10.1007/s00603-025-05177-1.
[23] Y. Lu, Y. Yu, G. Feng, D. Geng, J. Zeng, H. Zheng, Experimental study on dynamic mechanical response and crack control mechanism of anchored layered sandstone by DIC technology, Measurement 250 (2025) 117078, https://doi.org/10.1016/j.measurement.2025.117078.
[24] X. Sun, L. Wang, M. Jiang, C. Miao, Y. Zhang, B. Li, Experimental and numerical study on the mechanical behavior of layered rock anchored by CRLD anchor cable, Eng. Fail. Anal. 165 (2024) 108773, https://doi.org/10.1016/j.engfailanal.2024.108773.
[25] J. Ma, D. Li, P. Luo, C. Zhang, F. Gao, Dynamic damage and failure of layered sandstone with pre-cracked hole under combined cyclic impact and static loads, Rock Mech. Rock Eng. 56 (2022) 2271–2291, https://doi.org/10.1007/s00603-022-03170-6.
[26] Z. Wang, C. Rong, Q. Su, Y. Li, Study on the dynamic mechanical properties and crack evolution characteristics of layered gneiss with filled joints, Structures 79 (2025) 109499, https://doi.org/10.1016/j.istruc.2025.109499.
[27] J. Li, W. Yuan, H. Li, C. Zou, Study on dynamic shear deformation behaviors and test methodology of sawtooth-shaped rock joints under impact load, Int. J. Rock Mech. Min. Sci. 158 (2022) 105210, https://doi.org/10.1016/j.ijrmms.2022.105210.
[28] R. Bi, C. Xu, M. Liu, K. Du, Failure mechanisms and mechanical behavior of wedge-containing tunnel roof rock mass under biaxial loading, Int. J. Min. Sci. Technol. 35 (2025) 1107–1127, https://doi.org/10.1016/j.ijmst.2025.06.002.
[29] J.-C. Yu, J.-T. Wang, J.-W. Pan, N. Guo, C.-H. Zhang, A dynamic FEM-DEM multiscale modeling approach for concrete structures, Eng. Fract. Mech. 278 (2023) 109031, https://doi.org/10.1016/j.engfracmech.2022.109031.
[30] H. Zhong, Z. Yu, C. Zhang, L. Lyu, L. Zhao, Dynamic mechanical responses of reinforced concrete pier to debris avalanche impact based on the DEM-FEM coupled method, Int. J. Impact Eng 167 (2022) 104282, https://doi.org/10.1016/j.ijimpeng.2022.104282.
[31] M. Fattahi, M. Malekshahi, A. Permanoon, Mesoscale numerical modeling of unreinforced masonry wall response to underground dynamic loads: a comparative study utilizing FEM and DEM, Structures 63 (2024) 106460, https://doi.org/10.1016/j.istruc.2024.106460.
[32] S. Deng, Y. Yan, X. Wang, Z. Ma, Dynamic mechanical behavior and failure characteristics of jointed rock-like specimen under impact load, Eng. Fail. Anal. 167 (2025) 108975, https://doi.org/10.1016/j.engfailanal.2024.108975.
[33] H. Xie, W.G. Pariseau, Fractal estimation of joint roughness coefficients, Int. J. Rock Mech. Min. Sci. Geomech. Abstr. 30 (1993) A152, https://doi.org/10.1016/0148-9062(93)92841-d.
[34] F. Ren, T. Huang, C. Zhu, M. Karakus, Y. Jiang, Y. Chang, Mechanical behaviors and anchoring mechanism of coal-rock-bolt combinations under high strain rate conditions, J. Rock Mech. Geotech. Eng. 17 (2025) 7221–7236, https://doi.org/10.1016/j.jrmge.2025.01.049.
[35] H. Kang, J. Yang, F. Gao, J. Li, Experimental study on the mechanical behavior of rock bolts subjected to complex static and dynamic loads, Rock Mech. Rock Eng. 53 (2020) 4993–5004, https://doi.org/10.1007/s00603-020-02205-0.
[36] H. Ledbetter, Dynamic vs. static Young's moduli: a case study, Mater. Sci. Eng. A 165 (1993) L9–L10, https://doi.org/10.1016/0921-5093(93)90634-Q.
[37] F. Dai, S. Huang, K. Xia, Z. Tan, Some fundamental issues in dynamic compression and tension tests of rocks using split Hopkinson pressure bar, Rock Mech. Rock Eng. 43 (2010) 657–666, https://doi.org/10.1007/s00603-010-0091-8.
[38] T. Chen, S. Xu, B. He, Y. Li, H. Lei, Mechanical response of tunnel surrounding rock under blasting disturbance with different stress conditions based on acoustic emission and digital image correlation, Eng. Geol. 357 (2025) 108354, https://doi.org/10.1016/j.enggeo.2025.108354.
[39] H. Su, X. Qin, Y. Feng, L. Yu, Z. Sun, Experimental investigation of mixed mode I-II fracture property of thermally treated granite under dynamic loading, Theor. Appl. Fract. Mech. 118 (2022) 103267, https://doi.org/10.1016/j.tafmec.2022.103267.
[40] J. Blaber, B. Adair, A. Antoniou, Ncorr: Open-source 2D digital image correlation MATLAB software, Exp. Mech. 55 (2015) 1105–1122, https://doi.org/10.1007/s11340-015-0009-1.
[41] J. Wang, L. Ma, F. Zhao, B. Lv, W. Gong, M. He, P. Liu, Dynamic strain field for granite specimen under SHPB impact tests based on stress wave propagation, Undergr. Space 7 (2022) 767–785, https://doi.org/10.1016/j.undsp.2021.11.010.
[42] W. Yao, Z. Lei, J. Wang, L. Zhu, B. Wu, Stress wave propagation and transmission coefficients in jointed rock specimens with various surface roughness, Rock Mech. Rock Eng. (2025), https://doi.org/10.1007/s00603-025-04849-2.
[43] S. Zhang, H. Luan, Y. Jiang, Y. Wang, B. Li, Z. Liu, T. Jiang, X. Li, Study on the load transfer and damage evolution characteristics of the bolt-grout interface concerning bolt rib parameters: based on a Finite-Discrete numerical method, Comput. Geotech. 179 (2025) 107010, https://doi.org/10.1016/j.compgeo.2024.107010.
[44] D. Wu, H. Su, L. Yu, S. Geng, Z. Sun, T. Zhang, W. Li, Influences of bedding properties on the mixed-mode fracture behavior of shale under different dynamic loadings, Eng. Fract. Mech. 325 (2025) 111337, https://doi.org/10.1016/j.engfracmech.2025.111337.
[45] R. Cao, H. Yu, X. Qiu, H. Lin, M. Cao, Influence of loading rate on the mode II fracture characteristics of SCC samples: Experiments and numerical simulations, Theor. Appl. Fract. Mech. 134 (2024) 104729, https://doi.org/10.1016/j.tafmec.2024.104729.
[46] Z. Han, Z. Yan, D. Li, H. Wang, H. Wang, Dynamic fracture mechanism from a pre-existing flaw in granite: Insights from grain-based modelling, Soil Dyn. Earthq. Eng. 184 (2024) 108810, https://doi.org/10.1016/j.soildyn.2024.108810.
[47] Z. Wang, J. Fu, J. Wang, S. Li, C. Feng, Numerical study on dynamic behavior and microscopic damage mechanism of 3D printed rock-like materials, Comput. Geotech. 173 (2024) 106495, https://doi.org/10.1016/j.compgeo.2024.106495.
[48] S. Wen, R. Huang, C. Zhang, X. Zhao, Mechanical behavior and failure mechanism of composite layered rocks under dynamic tensile loading, Int. J. Rock Mech. Min. Sci. 170 (2023) 105533, https://doi.org/10.1016/j.ijrmms.2023.105533.
[49] J. Huo, C. Zhu, X. Chen, J. Guo, H. Jiao, L. Zhang, Y. Xu, M. Wang, X. Jin, Research on dynamic mechanical properties and numerical simulation of broken coal-rock grouting consolidation bodies, Results Eng. 26 (2025) 105404, https://doi.org/10.1016/j.rineng.2025.105404.
[50] Y. Zhou, J. Zhang, S. Yu, F. Wu, Effect of inclination angle and fissure spacing on the dynamic fracturing processes of X-shaped fissured specimens: Insights from SHPB experiments and DEM-FDM simulations, Theor. Appl. Fract. Mech. 142 (2026) 105404, https://doi.org/10.1016/j.tafmec.2025.105404.
[51] T. Zhang, Z. Zhu, Y. Ma, Z. Cheng, T. Li, Rate-dependent FDEM numerical simulation of dynamic tensile fracture and failure behavior in frozen soil, Comput. Geotech. 178 (2025) 106916, https://doi.org/10.1016/j.compgeo.2024.106916.
[52] C. Chen, P. Geng, Q. Yang, Y. Zhao, W. Gu, C. He, J. Zhang, Dynamic constitutive modeling of steel fiber reinforced concrete considering damage evolution under high strain rate, Constr. Build. Mater. 440 (2024) 137433, https://doi.org/10.1016/j.conbuildmat.2024.137433.

[53] R. Guo, J. Dong, L. Ma, Z. Long, F. Xu, C. Yin, Three-dimensional mesoscopic investigation on the dynamic compressive behavior of coral sand concrete with reinforced granite coarse aggregate (GCA), Compos. Struct. 352 (2025) 118650, https://doi.org/10.1016/j.compstruct.2024.118650.
[54] W. Tang, C. Zhai, X. Yu, J. Xu, Y. Sun, Y. Cong, Y. Zheng, Y. Wang, Dynamic Brazilian splitting experiment of bedding shale based on continuum-discrete coupled method, Int. J. Impact Eng 168 (2022) 104289, https://doi.org/10.1016/j.ijimpeng.2022.104289.
[55] K. Xia, Y. Zhou, W. Yao, J. Li, Z.-X. Zhang, I. Canbulat, X. Li, H. Li, Q. Zhang, Z. Zhou, S. Cho, K. Uenishi, T. Backers, J. Zhao, ISRM suggested methods for determining the rate-dependent shear strength and mode II fracture toughness of rock materials using the split Hopkinson pressure bar (SHPB), Rock Mech. Rock Eng. (2025), https://doi.org/10.1007/s00603-025-04972-0.
[56] M.F. Waqar, S. Qi, B. Zheng, S. Guo, Dynamic testing methods and failure properties of rocks: a comprehensive review, Rock Mech. Rock Eng. (2025), https://doi.org/10.1007/s00603-025-05069-4.
[57] J. Yang, T. Yu, Z. Ye, Y. Zou, C. Zhou, Numerical and experimental investigation into dynamic fracture and energy dissipation of red sandstone under multi-axial confining pressure, Tunn. Undergr. Space Technol. 158 (2025) 106446, https://doi.org/10.1016/j.tust.2025.106446.
[58] E.G. Kakouris, S.P. Triantafyllou, Phase-Field material point method for dynamic brittle fracture with isotropic and anisotropic surface energy, Comput. Methods Appl. Mech. Eng. 357 (2019) 112503, https://doi.org/10.1016/j.cma.2019.06.014.
[59] Q. Wu, H. Xiao, L. Weng, Y. Yang, Z. Ye, S. Wang, M. Tao, Dynamic mechanical responses and cracking resistance effect of prestressed rockbolt subjected to impact loading, Int. J. Rock Mech. Min. Sci. 195 (2025) 106307, https://doi.org/10.1016/j.ijrmms.2025.106307.
[60] S. Wang, Y. Xu, K. Xia, T. Tong, Dynamic fragmentation of microwave irradiated rock, J. Rock Mech. Geotech. Eng. 13 (2021) 300–310, https://doi.org/10.1016/j.jrmge.2020.09.003.
[61] C. Wei, C.-M. Chan, W. Wu, X. Su, Y. Gu, M. Liu, Experimental investigation and discrete element modeling of acoustic emission characteristics, crack evolution, and energy variation in shale specimens during uniaxial compression, Results Eng. 28 (2025) 108317, https://doi.org/10.1016/j.rineng.2025.108317.
[62] Y. Guo, P. Chen, R. Liu, F. ZhijianYang, L. Zhang, K. Feng, B. Lv, G.H. Zhou, Compressibility and meso-mechanical behavior of polymer bonded explosives with different crystal qualities during pressing process, Compos. Struct. 354 (2025) 118784, https://doi.org/10.1016/j.compstruct.2024.118784.
[63] A. Keneti, B.-A. Sainsbury, Review of published rockburst events and their contributing factors, Eng. Geol. 246 (2018) 361–373, https://doi.org/10.1016/j.enggeo.2018.10.005.
[64] T. Zhang, L. Yu, Y. Peng, H. Jing, H. Su, J. Wei, Effect of the mineral spatial distribution heterogeneity on the tensile strength of granite: Insights from PFC3D-GBM numerical analysis, J. Rock Mech. Geotech. Eng. 15 (2023) 1144–1160, https://doi.org/10.1016/j.jrmge.2022.07.012.
[65] Z. Han, K. Liu, J. Ma, D. Li, Numerical simulation on the dynamic mechanical response and fracture mechanism of rocks containing a single hole, Int. J. Coal Sci. Technol. 11 (2024) 64, https://doi.org/10.1007/s40789-024-00718-5.
[66] S. Zhang, Y. Jiang, H. Luan, B. Li, J. Liu, C. Wang, Study on shear mechanical characteristics of rock joints under different anchorage lengths, Rock Mech. Rock Eng. 57 (2024) 9959–9981, https://doi.org/10.1007/s00603-024-04075-2.
[67] M. He, W. Zhang, W. Guo, Influence of angles between anchor rod and cracks on the bearing mechanism of anchored rocks: Insights from the perspective of AE, DSCM and IRT, Theor. Appl. Fract. Mech. 139 (2025) 105040, https://doi.org/10.1016/j.tafmec.2025.105040.
[68] Y. Shi, Q. Yin, M. He, Z. Tao, H. Zhang, W. Zha, Y. Ren, The role of dynamic normal disturbances on shear properties and failure behaviours of bolt anchorage systems, Eng. Fail. Anal. 182 (2025) 110096, https://doi.org/10.1016/j.engfailanal.2025.110096.
[69] L. Zheng, H. Tang, L. Wang, C. Li, C. Xiong, Z. Zou, C. Wang, L. Zhu, Y. Zhang, Long-term in situ monitoring of anchoring system and preliminary analysis of monitoring data, J. Earth Sci. (2026), https://doi.org/10.1007/s12583-024-0333-4.
[70] Y. Luo, Z. Shi, C. Wang, J. Chen, W. Liu, Y. Li, Y. Wu, Mechanical properties of rock bolt and analysis for the full-process of sliding failure based on rock mass absolute displacement, J. Traffic Transp. Eng. Engl. Ed. 9 (2022) 490–506, https://doi.org/10.1016/j.jtte.2020.11.001.
[71] A. Staniek, Technical problems and non destructive testing of rock bolt support systems in mines, Int. J. Coal Sci. Technol. 10 (2023) 6, https://doi.org/10.1007/s40789-023-00566-9.